Defining Cellular Diversity at the Swine Maternal-Fetal Interface Using Spatial Transcriptomics and Organoids

Cole R. McCutcheon[1], Allyson Caldwell[1], Liheng (Henry) Yang[1], Elisa Crisci[2], J. Alex Pasternak[3], Carolyn B. Coyne[1,4*]

1) Duke University School of Medicine, Department of Integrative Immunobiology, Durham, NC
2) Department of Population Health and Pathobiology, College of Veterinary Medicine, North Carolina State University, Raleigh, NC
3) Department of Animal Sciences, Purdue University, West Lafayette, IN
4) Duke Human Vaccine Institute, Durham, NC

*Address correspondence:
Carolyn Coyne, PhD
3130 Medical Sciences Research Building III
3 Genome Court
Durham, NC 27710
USA
carolyn.coyne@duke.edu

ABSTRACT

The placenta is a dynamic, embryo-derived organ essential for fetal growth and development. While all eutherian mammals have placentas composed of fetal-derived trophoblasts that mediate maternal-fetal exchange, their anatomical and histological structures vary across species due to evolutionary divergence. Despite the cellular heterogeneity of porcine trophoblasts *in vivo*, understanding the mechanisms driving porcine placental development has been limited by the lack of *in vitro* models replicating this heterogeneity. In this study, we derived swine trophoblast organoids (sTOs) from full-term porcine placentas, retaining key transcriptional signatures of *in vivo* trophoblasts. To identify conserved cell populations, we integrated Visium spatial transcriptomics from mid-gestation porcine placentas with single-cell transcriptomics from sTOs. Spatial transcriptomics revealed novel markers of the porcine uterus and placenta, enabling precise separation of histological structures at the maternal-fetal interface. The integration of tissue and sTO transcriptomics showed that sTOs spontaneously differentiate into distinct trophoblast populations, with conserved gene expression and cell communication programs. These findings demonstrate that sTOs recapitulate porcine placental trophoblast populations, offering a powerful model for advancing placentation research. Our work also provides a spatially resolved whole-transcriptome dataset of the porcine maternal-fetal interface, opening new avenues for discoveries in placental development, evolution, and health across mammals.

63 **INTRODUCTION**

64 The defining feature of eutherian mammals is the presence of the fetal derived placenta.
65 The placenta is critical for fetal growth due to its numerous functions ranging from nutrient
66 transfer[1,2], steroidogenesis[3], and immunological defense[4,5]. While these placental functions are
67 largely maintained across species, the placenta has repeatedly evolved via a combination of
68 convergent and divergent evolution resulting in variable placental morphologies across species[6,7].

69 Placental structure is commonly categorized by the tissue layers separating the maternal
70 and fetal vasculature[7,8]. In the most invasive placental type, termed hemochorial, the placenta
71 erodes the uterine epithelium and remodels the uterine vasculature resulting in the influx of
72 maternal blood which directly bathes the placental epithelial cells, termed trophoblasts [7]. This type
73 of placentation is observed in many species including humans and rodents. Conversely, porcine
74 placentae are considered the least invasive placental type, termed epitheliochorial. In this system
75 the uterine vasculature, stroma and epithelium remain intact due to a lack of invasion by the
76 trophoblast cells [7]. In this case, the primary contact point for the placenta is the uterine epithelium.
77 Critically, regardless of the placental type or structure, all gas and nutrient transfer must occur
78 across the trophoblast layer [9].

79 In humans, trophoblasts consist of several subpopulations[10-12]. The three primary classes
80 of trophoblasts include cytotrophoblasts (CTBs), extravillous trophoblasts (EVTs), and the
81 multinucleated syncytiotrophoblast (STB). CTBs represent the mononuclear, proliferative,
82 undifferentiated trophoblast population of the placenta[10] whereas EVTs are highly invasive,
83 immunosuppressive cells, that primarily serve to remodel the maternal spiral arteries[13-15].
84 Conversely, the STB is a terminally differentiated multinuclear trophoblast population that covers
85 the entire surface of the chorionic villi. They serve dual roles as both a barrier to infection and a
86 critical site layer for nutrient and gas transfer[16,17].

87 Unlike human trophoblasts, which have been heavily characterized and subtyped[12,18], the
88 properties and subpopulations of swine trophoblasts are comparatively unknown, but several lines

89 of evidence suggest that subpopulations exist. First, the point of contact between the fetal
90 trophoblasts and uterine epithelium, termed the maternal-fetal interface, is extensively folded to
91 enhance placental surface area[19]. Along these folds, it has been reported that aquaporins [20] and
92 various transporters vary in expression[21], suggesting that trophoblast polarization along these
93 folds occurs. Second, the porcine placenta contains areolae, a cluster of specialized, columnar
94 trophoblast cells that sit atop uterine glands and facilitate the transfer of uterine gland secretions
95 to the developing fetus[22]. It is known that areolar trophoblasts are primed to uptake uteroferrin
96 compared to other trophoblasts[23] and express specific markers, such as cathepsin L1 (CTSL)[24],
97 suggesting a unique pattern of differentiation. Lastly, recent studies in early gestation porcine
98 placentas have revealed subpopulations of trophoblasts, which display unique expressional and
99 putative functions [25,26]. While these data serve as a critical advancement, these studies are unable
100 to spatially resolve these populations to known structures such as the interface or the areola,
101 thereby limiting the interpretation of these data [25,26].

102 Another major hurdle to furthering our understanding of porcine placentation is the lack of
103 suitable *in vitro* models. Limited access, coupled with high expense render *in vivo* and *ex vivo*
104 models challenging. While porcine trophoblast cell lines, such as PTr2[27,28], Jag-1[29], and pTR
105 cells[30] are available, these cells likely represent pre-implantation trophoblasts. Whether these cell
106 lines recapitulate later stages of placental development, or the cellular heterogeneity observed *in*
107 *vivo* remains unclear.

108 In human and murine systems, organoids have proven to be a valuable tool for studying
109 complex biological systems in part because they can be cryopreserved, are scalable, and are
110 often tractable[31]. Furthermore, as organoids spontaneously differentiate into various cell
111 populations, they represent one of the most physiologically relevant *in vitro* models[31]. We and
112 others have successfully derived trophoblast organoids from human and non-human primate
113 (NHP) placentas, demonstrating that they recapitulate the cellular heterogeneity and gene
114 expression patterns of the human and NHP placenta[32-37]. Because of the success of trophoblast

115 organoid models, we sought to develop a similar model of the swine placenta. Here, we show the
116 derivation of swine trophoblast organoids (sTOs) from full-term placental tissue. Our data
117 demonstrate that sTO can be expanded, passaged, and cryopreserved and recapitulate the
118 expression of canonical markers of the swine placenta. Using Visium spatial transcriptomics of
119 mid-gestation swine placentas, we identified the gene signatures of diverse trophoblast
120 populations *in vivo* and identified novel maternal-fetal crosstalk pathways. By coupling spatial
121 transcriptomics of whole placentas with single-cell transcriptomics from sTO, we found that
122 organoids spontaneously differentiated into various trophoblast populations, accurately
123 replicating their gene signatures. Additionally, we identified gene changes along a differentiation
124 trajectory in sTOs, revealing signatures associated with the differentiation of distinct swine
125 trophoblast subpopulations. Taken together, these data demonstrate that sTO provide an
126 accurate and comprehensive model of the swine placenta, offering a powerful tool for advancing
127 studies of porcine placentation and reproductive biology *in vitro*.
128

129 **RESULTS**

130 **Derivation and long-term expansion of Swine Trophoblast Organoids**

131 To derive swine trophoblast organoids (sTOs), we collected full-term swine placenta tissue and
132 applied a similar two-step enzymatic digestion protocol used previously for the derivation of
133 human TOs (hTOs)[33] (**Figure 1A**). Isolated stem/progenitor cells were resuspended in Matrigel
134 and allowed to self-organize over a period of 7-10 days until spherical structures, reminiscent of
135 hTOs, were observed via brightfield microscopy (**Figure 1B, 1C**). Organoids were isolated from
136 initial wells by picking out single organoids, dissociated them, and then passaging using a
137 combination of enzymatic and mechanical dissociation. sTO growth was robust and scalable, with
138 an average propagation interval of 5-7 days. Unlike hTOs, which develop with "mini-cavities" at
139 their centers[32], sTOs exhibited a denser structure with no visible central cavities, which may reflect
140 species-specific differences in tissue architecture and cellular organization (**Figure 1C, 1D**).

141 Similar to hTOs, sTOs could be continuously passaged with no apparent phenotypic changes
142 (e.g., organoid size, morphology, growth kinetics) and can be cryopreserved and revived. We
143 successfully derived sTOs from five unique swine placentas with 100% success across all tissues
144 collected.

145 Having successfully derived sTO, we then sought to confirm their epithelial origin. To do
146 this we performed immunofluorescence staining for various known markers of the porcine
147 maternal-fetal interface. Notably, sTOs exhibited strong expression of the proliferation marker
148 MKI67 (**Figure 1E**), with heterogeneous staining intensity across cells. This pattern suggests a
149 transition from a highly proliferative state toward differentiation. Similarly, we found that sTO were
150 positive for the epithelial marker cytokeratin 18 (**Figure 1F**) and the tight junction marker ZO-1
151 (**Figure 1G**), both of which are known to be expressed by porcine trophoblasts. These data
152 suggest that sTO contain a highly proliferative population of epithelial cells derived from the
153 maternal-fetal interface.

154 A limitation of hTOs is their inverted polarity when grown in Matrigel "domes", resulting in
155 an inward-facing STB that does not accurately mimic the cellular polarity of the human placenta
156 *in vivo*[32]. To define the cellular orientation of sTOs, we performed immunostaining with the tight
157 junction marker ZO-1, which localizes to the apical surface of swine trophoblasts *in vivo* [38]. We
158 found that sTOs expressed ZO-1, which localized to the inner surface of organoids when grown
159 in Matrigel (**Figure 1G**). We showed previously that hTOs cultured in suspension grow with more
160 physiologic polarity, with the STB on the outer surface[32]. Using a similar approach, we found that
161 sTOs also reversed their polarity when grown in suspension for approximately 48 hours and that
162 ZO-1 relocalized to the organoid outer surface (**Figure 1H**). sTOs grown in suspension also
163 displayed a more cystic morphology (**Figure 1I**). This suggests that the polarity of sTOs is easily
164 reversed, allowing for flexibility in experimental design.

165 To assess the ability of sTOs to recapitulate tissue-specific gene expression profiles, we
166 performed bulk RNA sequencing on sTOs. Using a previously established protocol for porcine

167 sex determination which relies on the expression of key Y-linked genes, we determined that sTO
168 were derived from both male and female placentae (**Figure 1J**)[39]. Having confirmed that sTO
169 were indeed fetal derived, we then compared their expressional profile to publicly available
170 expressional datasets of full-term porcine placental tissue, porcine uterine tissue, and PTr2 cells,
171 a commonly used *in vitro* model of swine trophoblasts. This approach allowed us to compare the
172 global transcriptional landscapes of organoids and their corresponding tissues, identifying key
173 expressional patterns to indicate how closely sTOs mimic the native tissue profile. This analysis
174 revealed that sTOs also express high levels of canonical swine trophoblast markers, at similar
175 levels to porcine placental tissue., whereas PTr2 cells exhibited very low levels of the same
176 markers (**Figure 1K**). Conversely, we found that while uterine tissues expressed high levels of
177 known uterine gland and fibroblast markers, sTO displayed an absence of expression of these
178 markers. While term placentas did exhibit some expression of fibroblast markers, they similarly
179 expressed an absence of uterine gland markers (**Figure 1K)**.Together, these data indicate that
180 sTO are composed of fetal-derived swine trophoblasts and display higher expression of these
181 markers than conventional models such as PTr2 cells.

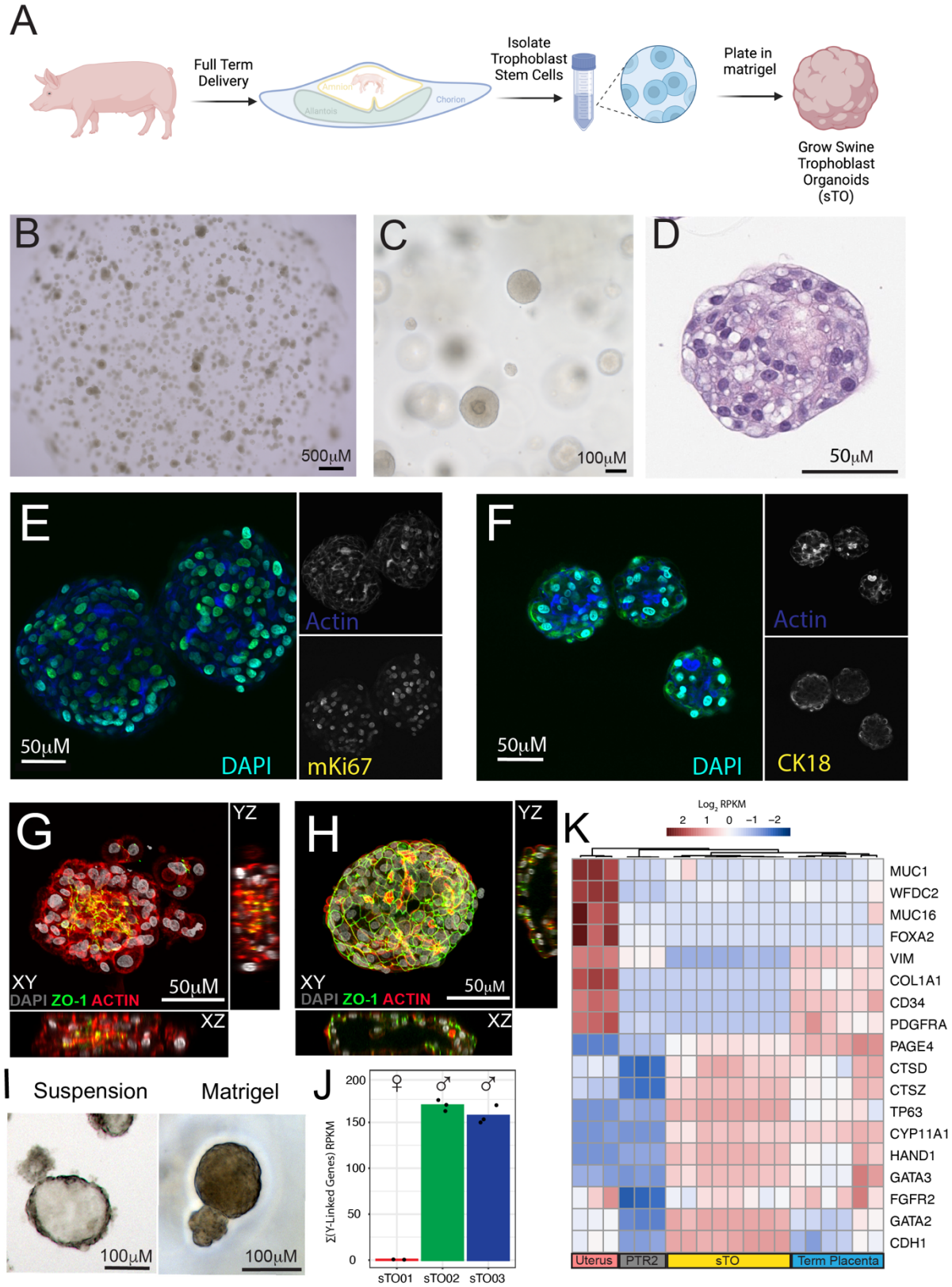
A
Full Term Delivery
Amnion
Allantois
Chorion
Isolate Trophoblast Stem Cells
Plate in matrigel
Grow Swine Trophoblast Organoids (sTO)
B
500μM
C
100μM
D
50μM
E
50μM
DAPI
Actin
mKi67
F
50μM
DAPI
Actin
CK18
G
YZ
XZ
XY
DAPI ZO-1 ACTIN
50μM
H
YZ
XZ
XY
DAPI ZO-1 ACTIN
50μM
I
Suspension
Matrigel
100μM
100μM
J
♀
♂
♂
Σ(Y-Linked Genes) RPKM
200
150
100
50
0
sTO01
sTO02
sTO03
K
Log2 RPKM
2 1 0 −1 −2
MUC1
WFDC2
MUC16
FOXA2
VIM
COL1A1
CD34
PDGFRA
PAGE4
CTSD
CTSZ
TP63
CYP11A1
HAND1
GATA3
FGFR2
GATA2
CDH1
Uterus
PTR2
sTO
Term Placenta

182

Figure 1: Establishment and validation of swine trophoblast organoids (sTO). A) Schematic of sTO derivation workflow. Created in BioRender. Mccutcheon, C. (2025) https://BioRender.com/ohwh6rx **B)** Representative low magnification brightfield image from a single well of sTO. **C)** High magnification brightfield image of sTO grown in Matrigel. **D)** Representative Hematoxylin and Eosin staining of a sectioned sTOs. **E-F)** Immunofluorescence microscopy image of sTO grown in matrigel stained with E) mKi67 and F) cytokeratin 18. **G)** Immunofluorescence microscopy image of sTO grown in Matrigel "domes". Apical marker ZO-1 is in green, DAPI in gray, and Actin in red. **H)** Immunofluorescence microscopy image of sTOs grown in suspension for 48 hours. Apical marker ZO-1 is in green, DAPI in gray, and Actin in red. **I)** Representative brightfield image of sTO grown in Matrigel "dome" (right) and suspension (left). J.) Bar-plot showing the average summation of RPKM for nine Y-linked genes across 3 individual sTO lines. Black dots indicate replicates. sTO lines are denoted on the x-axis. **I)** Heatmap of known pig placentae and uterus markers expressed across Uterus, PTr2 cells, sTOs, and term pig placentae. Individual columns indicate replicates. Clustering of columns is performed using hierarchical clustering, which groups columns with similar expressional patterns.

Single-cell Transcriptional Profiling Reveals Cellular Heterogeneity in sTOs

To determine whether sTOs differentiated into multiple trophoblast lineages, we next performed single-cell RNA-sequencing on three unique lines of sTOs. This analysis revealed five cell clusters (**Figure 2A**), with similar proportions across lines (**Figure 2B**). Canonical trophoblast markers including KRT7, KRT18, KRT8, CDH1, GATA2, HAND1, TP63, and GATA3 were highly expressed in sTOs (**Figure 2C**) with low expression of the fibroblast markers VIM, PDGFRA, and COL1A1 (**Figure 2D**). Similarly, we observed very low expression of the uterine gland markers FOXA2, MUC16, MUC1, and CD36 (**Figure 2D**). Taken together these data indicate that sTO are a pure population of trophoblasts that do not contain fibroblasts or glandular epithelial cells. Cluster gene expression enrichment analysis revealed that trophoblast clusters were discernable by cluster-specific gene expression (**Figure 2E, Supplemental Table 1**). For example, cluster 0 was enriched with transcripts such as SOX5 and WNT6, cluster 1 had enriched expression of tight junction-associated genes OCLN and CLDN1, cluster 2 was marked by cell proliferation genes like TOP2A, cluster 3 showed high expression of inflammatory genes including CXCL8 and interferon-stimulated genes (ISGs), and cluster 4 exhibited elevated levels of COX enzymes (**Figure 2E**). Previous studies using *in situ* hybridization, antibody staining, and single cell transcriptomics have identified markers of both swine interface trophoblasts and areolar

217 trophoblasts[20,24,25,40,41]. While we observed expression of these markers within sTO cell
218 populations, they did not fully segregate the trophoblast populations, ultimately limiting the utility
219 of these markers to define the cellular identity of sTO-derived clusters (**Figure 2F**). Of note, we
220 did observe that known pan-trophoblast markers such as CTSB and KRT18 were uniformly
221 expressed in sTOs suggesting that these various sTO cell populations are distinctive lineages
222 rather than contaminating cell populations (**Figure 2G**). While this analysis identified several
223 trophoblast populations in sTOs, the lack of a comprehensive marker list specific to the swine
224 maternal-fetal interface made it difficult to definitively assign cellular identities to these clusters.

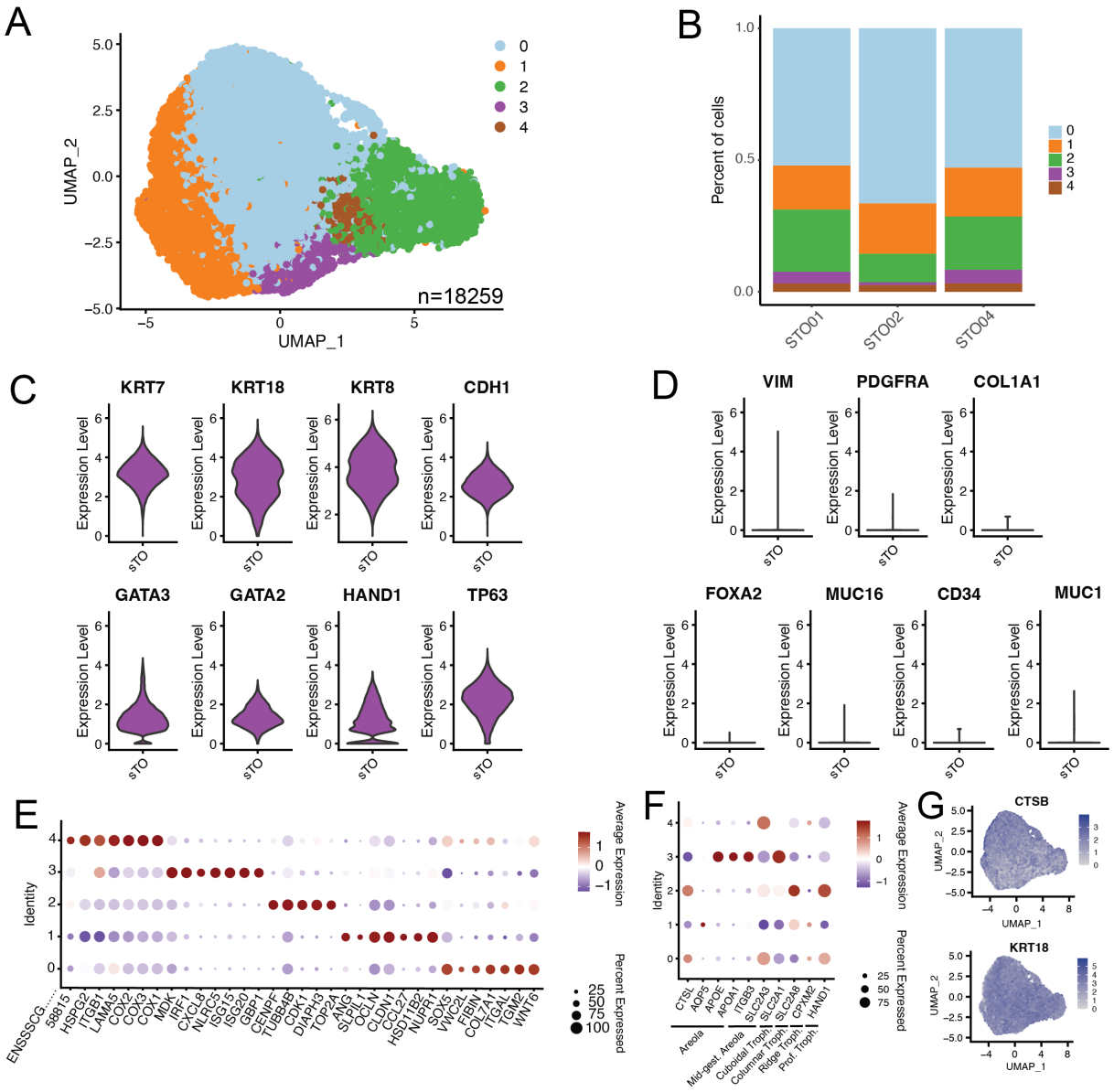

Figure 2: Single-cell transcriptomics of sTOs reveals cellular heterogeneity. A) UMAP from single cell transcriptomics of 3 independent lines of sTOs. **B)** Stacked bar-plot showing the relative proportions of various cell populations across three sTO lines. **C)** Violin plot showing the expression of canonical trophoblast markers in sTO single cell data. **D)** Violin plot showing the expression of canonical fibroblast markers in sTO single cell data. **E)** Dot-plot showing the top enrichment markers for various cell populations in sTOs. Color of dots denote average expression, whereas size represents percentage of cells in a cluster expressing the gene of interest. **F)** Dot-plot of canonical markers of various porcine trophoblast populations. Color of dots denote average expression, whereas size represents percentage of cells in a cluster expressing the gene of interest. **G)** Feature plot showing widespread expression of pan-trophoblast markers in sTOs.

238 **Visium-Based Spatial Transcriptomics Reveals Cellular Architecture at the Swine**
239 **Maternal-Fetal Interface**

240 To define the transcriptional signature of various cell populations comprising the porcine maternal-
241 fetal interface, we utilized Visium spatial transcriptomics, which allows for high-resolution spatial
242 mapping of gene expression. We applied this approach to mid-gestation maternal-fetal interfaces
243 (uterus with attached placenta) from four separate pregnancies (2 male and 2 female), enabling
244 the precise localization of gene expression patterns within the tissue architecture (**Figure 3A**).
245 Our analysis identified 10 distinct cell populations among the four placentae analyzed (**Figure**
246 **3B, Supplemental Figure 1A**). To assign cellular and regional identities to these clusters, we
247 utilized a combination of known marker expression (**Figure 3C**), histology (**Figure 3D**), and
248 cluster-specific gene enrichment analysis (**Supplemental Table 2**). Notably, the maternal and
249 fetal compartments were also discernable using this clustering technique (**Figure 3E,**
250 **Supplemental Figure 1B**). The maternal compartment was divided into six clusters: the
251 myometrium, represented by clusters 0 (Myo-1) and 6 (Myo-2); the endometrium, represented by
252 cluster 1 (Endo); blood and blood vessels, represented by clusters 7 (Blood) and 4 (Vasc); and
253 the uterine epithelium, represented by cluster 3 (UtEp) (**Figure 3D, 3F, Supplemental Figure**
254 **1C**). The fetal compartment was divided into four cell populations: the interface trophoblasts,
255 represented by cluster 5 (IntTroph); the areolae, represented by clusters 8 (Areola-1) and 9
256 (Areola-2); and the interstitium, represented by cluster 2 (Ist) (**Figure 3D, 3F, Supplemental**
257 **Figure 1C**). We observed some degree of sample-to-sample variability, which stemmed primarily
258 from differences in both cellular makeup and tissue structure between sections (**Figure 3G**).
259 Myometrium clusters were primarily defined by the expression of smooth muscle markers,
260 including SMTN, CNN1, ACTG2, MYL9, and MYLK. Blood vessels were characterized by the
261 expression of CLDN11 and CCL21, while blood cells were classified by high levels of ALAS2 and
262 HBM (**Figure 3C**). The endometrium was marked by elevated expression of SLPI and MEP1B,
263 both well-known to be expressed in this tissue (**Figure 3C**). Uterine epithelial cells expressed high

levels of established markers IGFBP2 and IGFBP3, whereas interface trophoblasts showed elevated expression of pregnancy-stimulated genes (PSGs), PAGE4, PAG2L4, and HSD3B1 (**Figure 3C**). The interstitium cluster was defined by the expression of APOE, PEG10, DLK1, and GPC3 (**Figure 3C**). Finally, the areola clusters were divided into two histologically and transcriptionally distinct populations: Areola-1, characterized by high CTSL expression, and Areola-2, with moderate CTSL expression. Areola-1 also expressed high levels of LIF and MMP25, while Areola-2 was distinguished by elevated expression of LRP2, CYP11A1, and MMP7 (**Figure 3C, 3H**). Where Areola-2 displayed a structure that is continuous with the interface trophoblasts, Areola-1 did not appear to be continuous with the interface trophoblasts (**Figure 3D, 3H, Supplemental Figure 1C**), suggesting these distinct structures may have different functions.

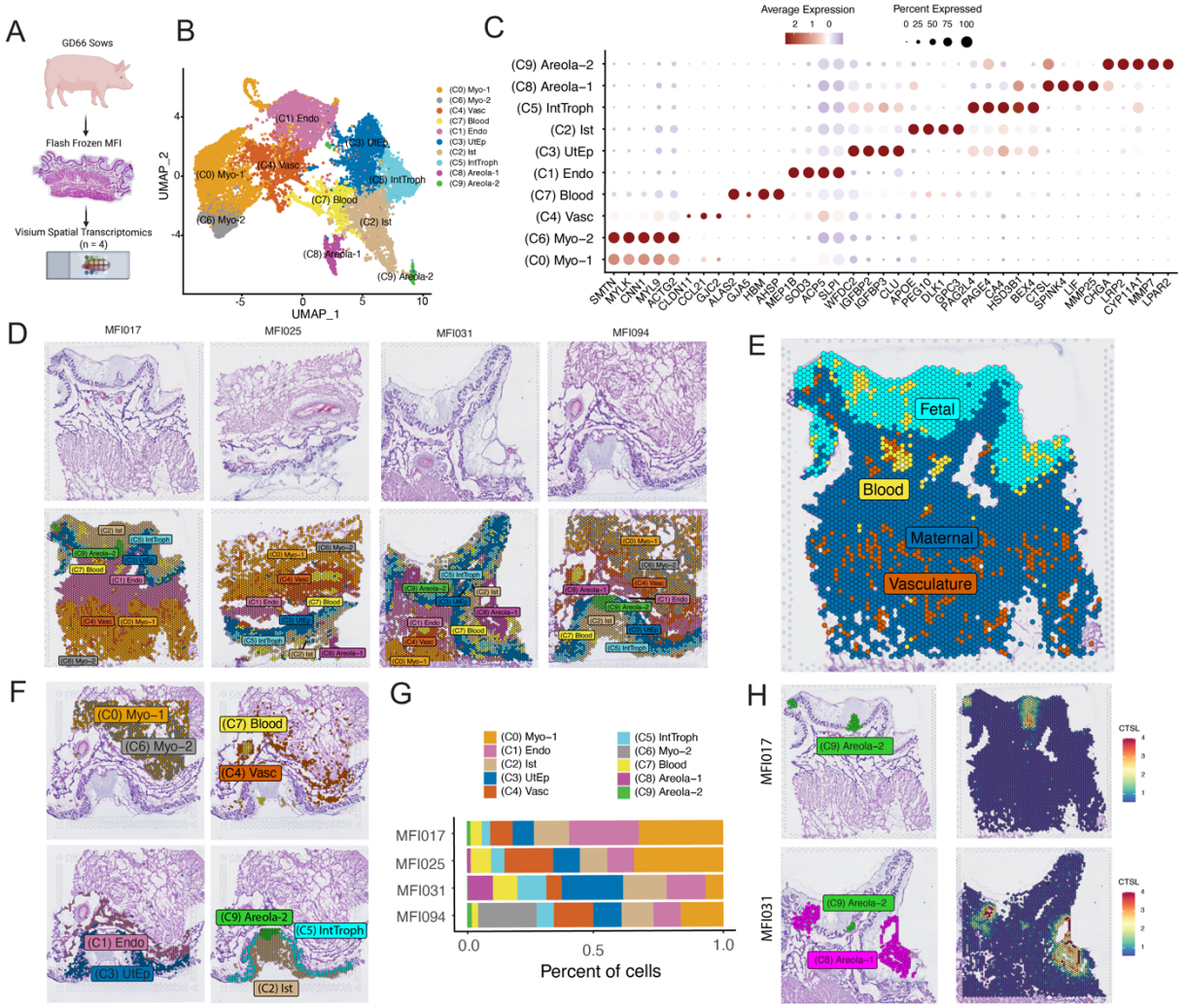

Figure 3: Spatial Transcriptomics Resolves Global Expression at the Porcine Maternal-Fetal Interface. A) Schematic of spatial transcriptomics workflow of gestational day 66 (GD66) maternal fetal interfaces (n = 4; 2 male and 2 female). Created in BioRender. Mccutcheon, C. (2025) https://BioRender.com/hus6ktj **B)** UMAP showing 10 distinct populations obtained via spatial transcriptomics. **C)** Dot-plot of top markers for each cluster obtained via spatial transcriptomics. Color of dots denote average expression, whereas size represents percentage of cells in a cluster expressing the gene of interest. **D)** H&E staining of individual porcine maternal-fetal interface sections (top). Spatial DimPlot showing the histologic localization of UMAP cluster populations (bottom). Each image represents a separate maternal-fetal interface. **E)** Spatial Dim-plot showing separation of maternal and fetal compartments. Representative maternal-fetal Interface shown. **F)** Spatial Dim-Plot showing the histologic localization of UMAP individual cluster populations. Representative maternal-fetal Interface shown (MFI094). **G)** Stacked bar-plot showing the relative proportion of each cluster across individual maternal-fetal interfaces. **H)** Spatial DimPlot (Left panels) and Spatial Feature plots (Right panels) showing the localization of areola-1 and areola-2 structures (Left panels) and the expression of CTSL (right panels) within representative maternal-fetal interfaces.

Defining Cellular Markers at the Swine Maternal-Fetal Interface Through Spatial Transcriptomics

Using the spatial transcriptomics dataset described above, we analyzed the cellular and molecular landscape of the swine maternal-fetal interface to identify distinct markers associated with specific cell types and regions. This approach enabled us to map the spatial distribution of key genes, including those enriched in select trophoblast populations. To identify trophoblast specific markers, we performed differential expression analysis between clusters containing trophoblasts, (clusters 5, 8 and 9) and all other clusters. This analysis revealed both pan-trophoblast markers, and markers of specific trophoblast populations (**Figure 4A, 4B, Supplemental Figure 2A-E**). Specifically, the genes encoding cathepsin Z (CTSZ) and cathepsin B (CTSB) were highly expressed in both interface trophoblasts as well as areolae trophoblasts, but only weakly expressed elsewhere (**Figure 4A, 4B, Supplemental Figure 2A**). Similarly, the genes encoding carbonic anhydrase 4 (CA4) and pregnancy associated glycoprotein L4 (PAG2L4) demarcated interface trophoblasts (**Figure 4A, 4B, Supplemental Figure 2B**). Areolar trophoblasts universally expressed CTSL (**Figure 3H, Supplemental Figure 2C**); however, areola-1 trophoblasts specifically expressed coiled coil domain containing 162 (CCDC162) and serine peptidase inhibitor kazal type 4 (SPINK4) (**Figure 4A, 4B, Supplemental Figure 2E**).

Conversely, areola-2 trophoblasts were marked by an upregulation of matrix metalloprotease 7 (MMP7) and anterior gradient protein 2 homolog (AGR2) (**Figure 4A, 4B, Supplemental Figure 2D**). Notably, all of these highly specific markers were also detected within sTO, with varied expression levels across clusters, suggesting some degree of differentiation across sTO cell populations (**Figure 4C**). Although these markers partially resolved the clusters, their leaky expression across multiple clusters limited our ability to accurately assign cellular identities.

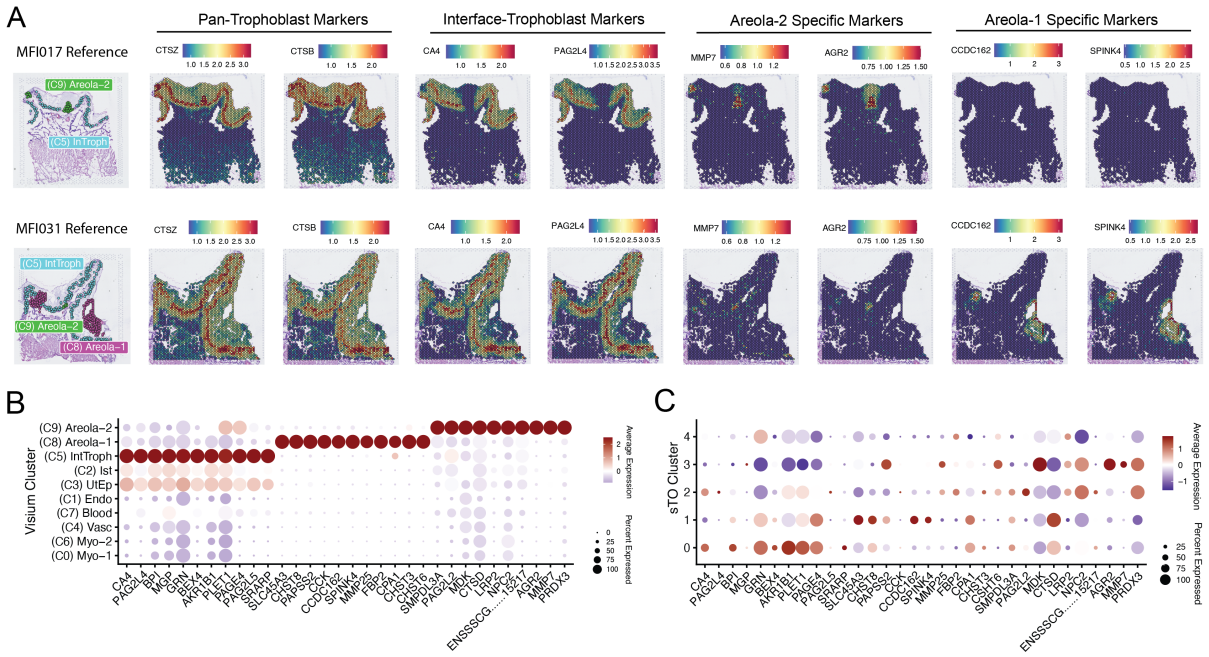

Figure 4: Spatial Transcriptomics Identifies Novel Trophoblast Specific Markers. A) Spatial FeaturePlots showing the localization of known or novel pan-trophoblast markers, interface-trophoblast markers, areola-2 and areola-1 specific markers. Two representative maternal-fetal interfaces are shown. The reference localization of these structures are shown on the far-left panels. **B)** DotPlot showing expanded markers of various trophoblast populations within the maternal-fetal interface. Color of dots denote average expression, whereas size represents percentage of cells in a cluster expressing the gene of interest. **C)** DotPlot showing the cluster specific expression of known and novel trophoblast markers from (B) in sTOs. Color of dots denote average expression, whereas size represents percentage of cells in a cluster expressing the gene of interest.

Characterizing Cell-Cell Interactions Within the Porcine Maternal-Fetal Interface Using Spatial Transcriptomics

330 Maternal-fetal crosstalk has been widely studied in human pregnancy, where it plays crucial roles
331 in nutrient exchange, immunological tolerance, and successful placentation[42-44]. Recent evidence
332 suggests that similar communication processes take place in the peri-implantation porcine
333 embryo and the maternal endometrium, highlighting the importance of defining these interactions
334 in the swine placenta[26,45]. To delineate communication networks at the swine maternal-fetal
335 interface, we used CellChat to define cell-cell signaling pathways. CellChat is based on a
336 comprehensive dataset of known ligand-receptor pairs, using their expression to infer
337 communication between cells. In spatially resolved data, CellChat also incorporates the physical
338 distance between tissue sites, filtering out interactions that are unlikely to occur due to the spatial
339 separation between these sites. Using this approach we found that the myometrium (Myo, which
340 was merged into a single cluster for this analysis) and the vasculature (Vasc) were responsible
341 for the most robust communication, while the interstitium (Ist), endometrium (Endo), Areola
342 (merged into a single cluster), and IntTroph showed the weakest number of communication
343 networks (**Figure 5A, 5B**). Notably, all maternal clusters were able to crosstalk with the fetal
344 trophoblast populations except the myometrium and vasculature. Using CellChat, we then
345 classified both outgoing and incoming signaling patterns. For outgoing signaling, pattern 1 and
346 pattern 2 were largely derived from the maternal compartment, with pattern 1 including the
347 endometrium and blood, whereas pattern 2 is primarily derived from the myometrium and
348 vasculature. Conversely, pattern 3 was shared among fetal-derived populations, including the Ist,
349 IntTroph, and Areola (**Figure 5C**). We similarly observed that incoming patterns were similarly
350 segregated by fetal and maternal compartments, with pattern 1 exhibiting the strongest signaling
351 for Areola, Ist, and IntTroph, and pattern 2 being composed of Myometrium, Vasculature, and
352 Blood (**Figure 5C**). Each pattern for the outgoing and incoming signaling networks corresponded
353 to distinct communication networks. For example, outgoing pattern 1 was dominated by OSTN,
354 VEGF, and BMP signaling, whereas pattern 3 was dominated by HGF, EGF, and CDH signaling.
355 Similar observations were made for incoming signaling patterns, with pattern 1 corresponding to

356 high levels of EGF, ANGPT, and GRN signaling, and pattern 2 being characterized by high levels
357 of NPR1, KIT, and CXCL signaling (**Figure 5C**). Notably, this compartmentalization of the
358 maternal and fetal signaling suggests that there is extensive maternal-fetal crosstalk occurring in
359 the porcine placenta. Some of these signals were unidirectional, with all outgoing signals deriving
360 from the maternal compartment, such as the HSPG signaling pathway, which is largely derived
361 from the myometrium and vasculature. Interestingly, this HSPG2 signal, which is important for
362 angiogenesis, is capable of being sensed by both the maternal system, and the interface
363 trophoblasts, largely due to the restriction of the receptor DAG1. In contrast, many crosstalk
364 pathways were enriched in various placenta trophoblast subpopulations. For example, the MK
365 pathway was restricted primarily to areola trophoblasts, whereas the IL6 pathway was largely
366 restricted to the interface trophoblasts. In both cases, the outgoing signal, MDK and IL6, were
367 localized to the areola and interface trophoblasts respectively. While the MDK receptor SDC2 was
368 broadly expressed in both the maternal and fetal compartment, IL6R was largely restricted to the
369 endometrium, with some lower-level expression in all other tissues. Interestingly, in both the MK
370 and IL6 pathways we observed some degree of inter-trophoblast communication, with interface
371 trophoblast and areolar trophoblasts displaying some degree of crosstalk. Together, these
372 findings highlight the extensive, bidirectional maternal-fetal crosstalk occurring at the porcine
373 maternal-fetal interface.
374
375
376

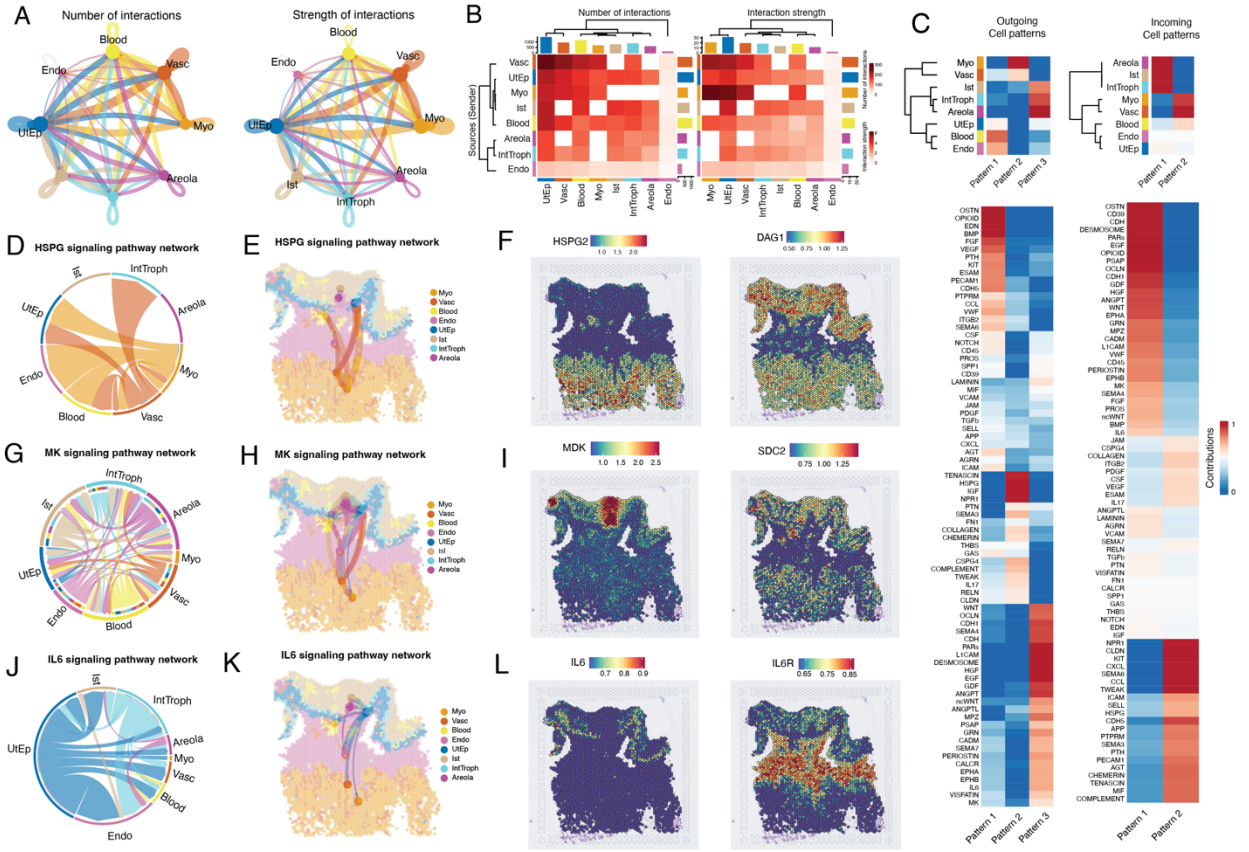

Figure 5: Cell-Cell Interactions Within the Porcine Placenta Maternal-Fetal Interface. **A)** Chord diagrams showing the number (Left panel) and strength (right panel) of calculated inter-cluster interactions within the porcine maternal-fetal interface. **B)** Heatmap showing the number (left panel) and strength (right panel) of interactions between clusters within the porcine maternal-fetal interface. Color indicates increased number (left) or strength (right) between the sending cluster and the receiving cluster. **C)** Heatmaps showing the outgoing (upper left panel) and Incoming (upper right panel) signaling patterns by cluster for Visium spatial transcriptomics. Coloring indicates relative cluster contribution to a pattern with red being high and blue being low contribution level. Lower panels similarly indicate the contribution a specific signaling pathway to the corresponding pattern designation with the lower right panel indicating outgoing signaling patterns and the lower left panel indicating incoming signaling patterns. **D-E)** Plots showing HSPG signaling within the porcine maternal-fetal interface, with **D)** being a chord diagram and **E)** showing the spatial localization of these interactions. **F)** Spatial feature plot showing the localization of various genes associated with the HSPG pathway. The right panel shows the localization of HSPG2, whereas the left panel shows the localization of DAG1. **G-H)** Plots showing MK signaling within the porcine maternal-fetal interface, with **G)** being a chord diagram and **H)** showing the spatial localization of these interactions. **I)** Spatial feature plot showing the localization of various genes associated with the MK pathway. The right panel shows the localization of MDK, whereas the left panel shows the localization of SDC2. **J-K)** Plots showing IL6 signaling within the porcine maternal-fetal interface, with **J)** being a chord diagram and **K)** showing the spatial localization of these interactions. **L)** Spatial feature plot showing the localization of various genes associated with the IL6 pathway. The right panel shows the localization of IL6, whereas the left panel shows the localization of IL6R.

401 **Cell Type Deconvolution of Trophoblast Populations in sTOs Using Spatial**
402 **Transcriptomics**

403 To define trophoblast populations within sTOs, we performed cell type deconvolution by
404 integrating the single-cell transcriptomics dataset from sTOs with the spatially resolved
405 transcriptome of the swine maternal-fetal interface. To do this, we filtered the Visium dataset to
406 only include trophoblast populations, specifically clusters 5, 8, and 9 (**Figure 6A-C**). Next, we
407 integrated the single cell RNA-sequencing data from sTO with the Visium spatial transcriptomics
408 dataset. For cell type prediction, we applied a previously established probabilistic modeling
409 algorithm, which leverages the likelihood of gene expression patterns across datasets to assign
410 cluster identities in a spatial context. This analysis enabled us to predict the identities of sTO
411 clusters with high confidence. We found that sTO cluster 0 very strongly mapped to interface
412 trophoblasts, whereas sTO clusters 1, 3, and 4 map to areola-2 and areola-1 trophoblast clusters
413 (**Figure 6D-E, Supplemental Figure 3A, 3B**). In contrast, cluster 2 did not exhibit strong mapping
414 to any structure (**Figure 6D, 6E, Supplemental Figure 3A, 3B**). However, this cluster expressed
415 high levels of the proliferation-associated genes TOP2A and MKI67, suggesting that it
416 represented the stem/progenitor cell population, which is likely present at very low abundance in
417 tissue at the stage of gestation when we were collecting the tissues (**Figure 6F**).

418 We then identified shared markers between sTO clusters and their corresponding spatial
419 transcriptomics clusters to determine the gene expression signatures that defined these
420 mappings. We found that sTO cluster 0 cells expressed 59 markers that were conserved in
421 interface-trophoblasts, which included AKR1B1, HAVCR1, C1QTNF4, and TGM2 (**Figure 6F, 6G,**
422 **Supplemental Table 3**). Similarly, sTO cluster 1 expressed 63 shared markers with areola-2
423 cluster, including cathepsins A and D (CTSA and CTSD), SLC7A4 and NUPR1 (**Figure 6F, 6G,**
424 **Supplemental Table 4**). sTO cluster 3 had 110 shared markers with areola-2 cluster, with both
425 clusters highly expressing ISG15, FTL, MDK, and B2M (**Figure 6F, 6G, Supplemental Table 5**).
426 Conversely, sTO cluster 4 expressed only 20 shared markers to areola-1 cluster, largely including

427 COX1, COX3, ND4, and CYTB (**Figure 6F, 6G, Supplemental Table 6**). Using this approach,
428 we were able to assign cellular identities and identify shared gene expression profiles for all
429 trophoblast populations within sTOs, which were distributed at similar ratios across independent
430 lines (**Figure 6H**). Taken together these data indicate that sTO are able to spontaneously
431 differentiate into various populations of trophoblasts found at the porcine maternal-fetal interface.
432
433

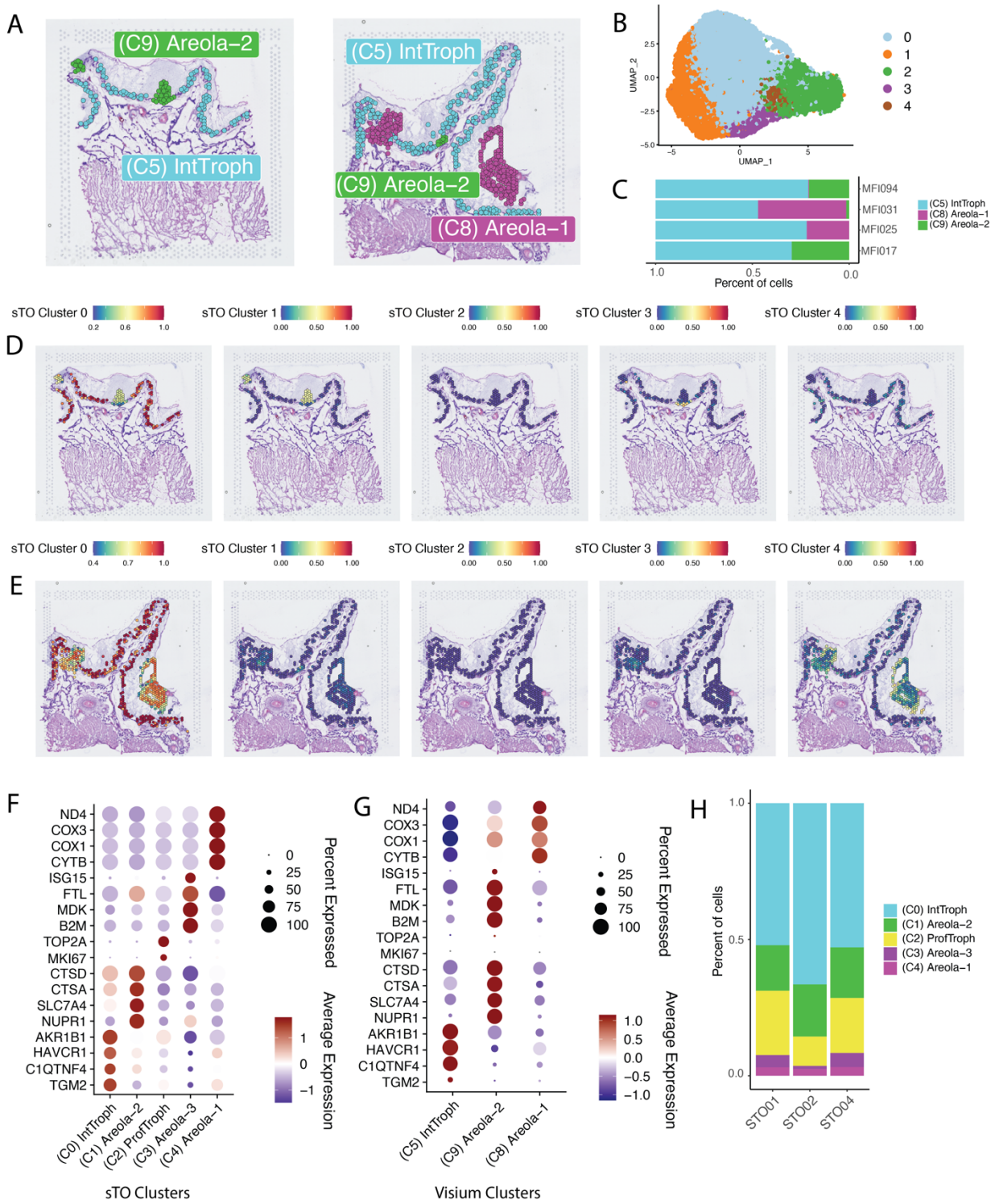

Figure 6: Integration of sTOs and Spatial Transcriptomics Datasets Enables Precise Cellular Identification and Classification. A) Spatial Dim-Plot showing facetted clusters from two representative maternal-fetal interfaces. As shown Areola-1, Areola-2 and Interface-Trophoblasts were included in this analysis. **B)** UMAP of sTOs clusters obtained via single cell

RNA-sequencing (n = 3 lines). **C)** Stacked bar-plot showing relative proportions of various clusters across individual maternal-fetal interfaces. **D-E)** Spatial feature plot showing prediction scores for each spot in the spatial dataset subsetted by sTO cluster. Color shown indicates probability that the classified sTO cluster is localized to a given position within the spatial dataset. **F-G)** Dot-plot showing the localization of shared markers between the sTO clusters (F) and maternal-fetal interface clusters (G) Color of dots denote average expression, whereas size represents percentage of cells in a cluster expressing the gene of interest. **H)** Stacked BarPlot showing the relative proportion and identity of sTO cell populations.

Pathway Analyses Reveals Conserved Functional Niches of sTO Cell Populations

In vivo, interface trophoblasts and areola trophoblasts have distinct functions. Our data indicated that sTOs differentiated into both of these populations, yet whether these populations retained the functional capacity of their *in vivo* counterparts remained unclear. To this end, we examined the functional pathways active in both sTOs and tissues across trophoblast subpopulations. Given that IntTroph and Areola-2 clusters had the highest probability scores and shared markers between sTO and tissue, we chose to focus this analysis on these two clusters. We performed differential expression analysis between interface trophoblasts and areola-2 trophoblasts, finding that expressional patterns between these two trophoblast populations were starkly different in both the tissue and sTO (**Supplemental Figure 4A, 4B**). Using GO-Term analysis we identified enriched pathways for areola-2 and interface trophoblasts, several of which were enriched in both sTOs and tissue analysis (**Supplemental Table 7-10)**. Notably, we found that interface trophoblasts are enriched in GO terms such as extracellular matrix, focal adhesions, and angiogenesis (**Supplemental Table 7, 9**). Conversely, areola-2 clusters were enriched primarily in GO terms surrounding endosome formation (**Supplemental Table 8, 10)**. Expression of various endosome related genes demonstrated that areola-2 clusters in sTOs and tissue Visium datasets are highly enriched in endosomal markers, whereas interface trophoblasts distinctly lack endosomal gene expression (**Supplemental Figure 4C,D)**. Taken together these data demonstrate that sTOs retain at least some key functions of the corresponding tissue populations, highlighting their utility for studying swine placental biology.

469 **Trajectory Inference Reveals Trophoblast Differentiation Pathways in sTOs**

470 Organoids provide a powerful model for defining differentiation trajectories, as they enable the
471 study of cell fate transitions from progenitor cells to more differentiated cell states in a controlled
472 environment. We applied Slingshot trajectory analysis to sTOs to trace the dynamic progression
473 of trophoblast cells along distinct developmental pathways. To do this, we first subsetted the sTOs
474 single-cell dataset to include major cell populations, which included proliferating trophoblasts
475 (ProfTroph), interface trophoblasts (IntTroph), and Areola-2 trophoblasts. We then performed
476 Slingshot trajectory analysis by first setting the starting point at the proliferating trophoblasts,
477 which displayed the highest expression of known stemness markers, including MKI67 and
478 TOP2A. We then allowed inference of downstream differentiation paths without further constraint.
479 This analysis revealed a single differentiation trajectory, starting in ProfTroph, progressing
480 through IntTroph, and terminating in Areola-2 (**Figure 7A**). To define gene expression changes
481 along this trajectory, we applied the fitGAM function to model dynamic gene expression patterns
482 to assess how specific gene expression profiles evolved across the different stages of trophoblast
483 differentiation. Many genes were temporally regulated along the trajectory, with some showing
484 distinct patterns of upregulation and downregulation, while others exhibited cyclical regulation
485 across the different stages of trophoblast differentiation (**Figure 7B, Supplemental Figure 5,**
486 **Supplemental Table 11**). Notably, TOP2A, HMGB2, and PRC1 were strongly downregulated
487 along the trajectory, suggesting a loss of a proliferative capacity as differentiation progresses
488 (**Figure 7B, 7C**). In contrast, GRN and ITM2C, both of which are known to be expressed in the
489 swine placenta, were markedly increased in expression in IntTroph, but then became
490 downregulated in the Areola-2 differentiated state (**Figure 7D, left**). Similarly, several genes
491 including NUS1, NUPRR1, SQSTM1, and ARF4 all increased in expression at the terminal areola-
492 2 differentiation stage (**Figure 7E, 7F**, left). To validate these findings from the trajectory analysis
493 of sTOs, we compared the gene expression patterns to the Visium spatial transcriptomics data.
494 This comparison revealed a high level of concordance between the temporally regulated markers

identified in sTOs and their expression in corresponding tissue structures, further confirming that sTOs effectively recapitulate the differentiation processes observed *in vivo* (**Figure 7D-F, Supplemental Figure 5A-F**).

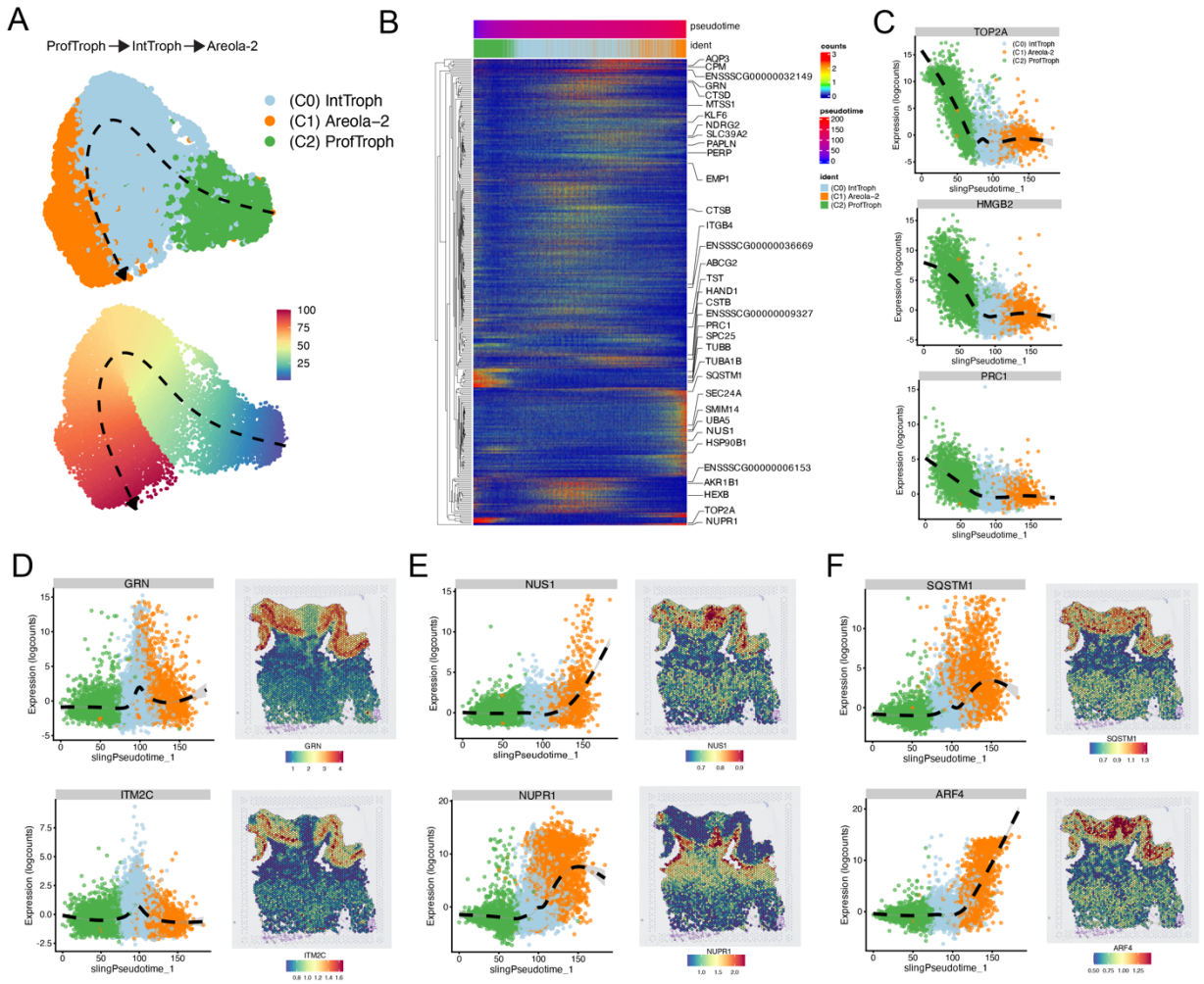

Figure 7: Trajectory Analysis Reveals the Differentiation Pathway of Swine Trophoblasts. A) UMAPs showing Slingshot calculated trajectory of trophoblasts within sTO. Top panel shows the trajectory across labeled clusters, whereas bottom panel shows the trajectory across a pseudotime. **B)** Heatmap showing temporally regulated genes across the calculated pseudotime trajectory. Individual columns represent individual cells that are ordered along the calculated pseudotime. Identities are positions along the pseudotime are shown above the heatmap. **C)** Representative expression plots showing gene expression changes along the calculated pseudotime that are enriched in the proliferative stem cell population. **D)** Representative expression plots and spatial feature plots showing genes that are enriched during the transition to Interface-Trophoblasts and their expression pattern within our spatial transcriptomics dataset. **E-F)** Representative expression plots and spatial feature plots showing genes that are enriched during the transition to Areola-2 trophoblasts and their expression pattern within our spatial transcriptomics dataset.

512

513

514 **Comparative Cell-Cell Interaction Network Analysis Identifies Preserved Communication**
515 **Networks Within sTOs and the Swine Placenta**

516 Crosstalk within the human placenta is well documented and controls processes such as fetal
517 development and immunological tolerance. Our data indicates that the porcine placenta similarly
518 displays a high level of intraplacental crosstalk, but additionally displays crosstalk between
519 various trophoblast subpopulations, including crosstalk between the areolar trophoblasts and
520 interface trophoblasts. Given that sTO contain both areolar and interface trophoblast populations,
521 we wanted to better characterize these inter-trophoblast crosstalk events within the porcine
522 placenta and assess how well these interactions are recapitulated in sTOs. To do this we first
523 subsetted both the Visium data and sTO datasets to only contain areolar trophoblast and interface
524 trophoblast subpopulations. For clarity areola trophoblast clusters were combined into a singular
525 cluster for each dataset. We then used Cellchat to assess cellular communication pathways
526 present between these populations. This analysis revealed extensive crosstalk in sTOs and in
527 tissue derived trophoblasts with substantial overlap in the signaling pathways between these
528 systems **(Figure 8A, 8B)**. Of note we found 28 shared signaling pathways between sTO and
529 tissue trophoblasts **(Figure 8A)**. In both sTO and and tissue trophoblasts we observed that
530 interface trophoblasts provide more substantial signaling than areolar trophoblasts (**Figure 8B**).

531 Patterning analysis revealed that the senders and receivers, were conserved across
532 several of these signaling pathways, suggesting concordance between sTO and tissue
533 trophoblast signaling (**Figure 8C-8F**). Some of these pathways displayed bidirectional crosstalk
534 between interface trophoblasts and areolar trophoblasts, such as the ANGPTL and CDH
535 pathways, which displayed extensive autocrine and paracrine signaling. The ANGPTL pathway
536 displayed a high degree of both autocrine and paracrine signaling between interface and areola
537 trophoblasts, primarily due to the widespread expression of integrins, syndecans, and ANGPTLs.

While we similarly found that areolar trophoblasts display both autocrine and paracrine signaling in the AGRN pathway, we found that interface trophoblasts do not display the same ability to signal in an autocrine manner, likely due to the lack of CDH4 expression. In contrast, we found that some pathways were cell type specific, such as the AGRN pathway, which is restricted to interface trophoblasts. While we detected high levels of DAG1 in both populations we found that AGRN was restricted largely to interface trophoblasts. Importantly, we found that in many of these pathways, including AGRN, CDH, and ANGPTL, displayed a high degree of similarity in signaling patterns between these systems highlighting the utility of sTO in studying inter-trophoblast communication in the placenta.

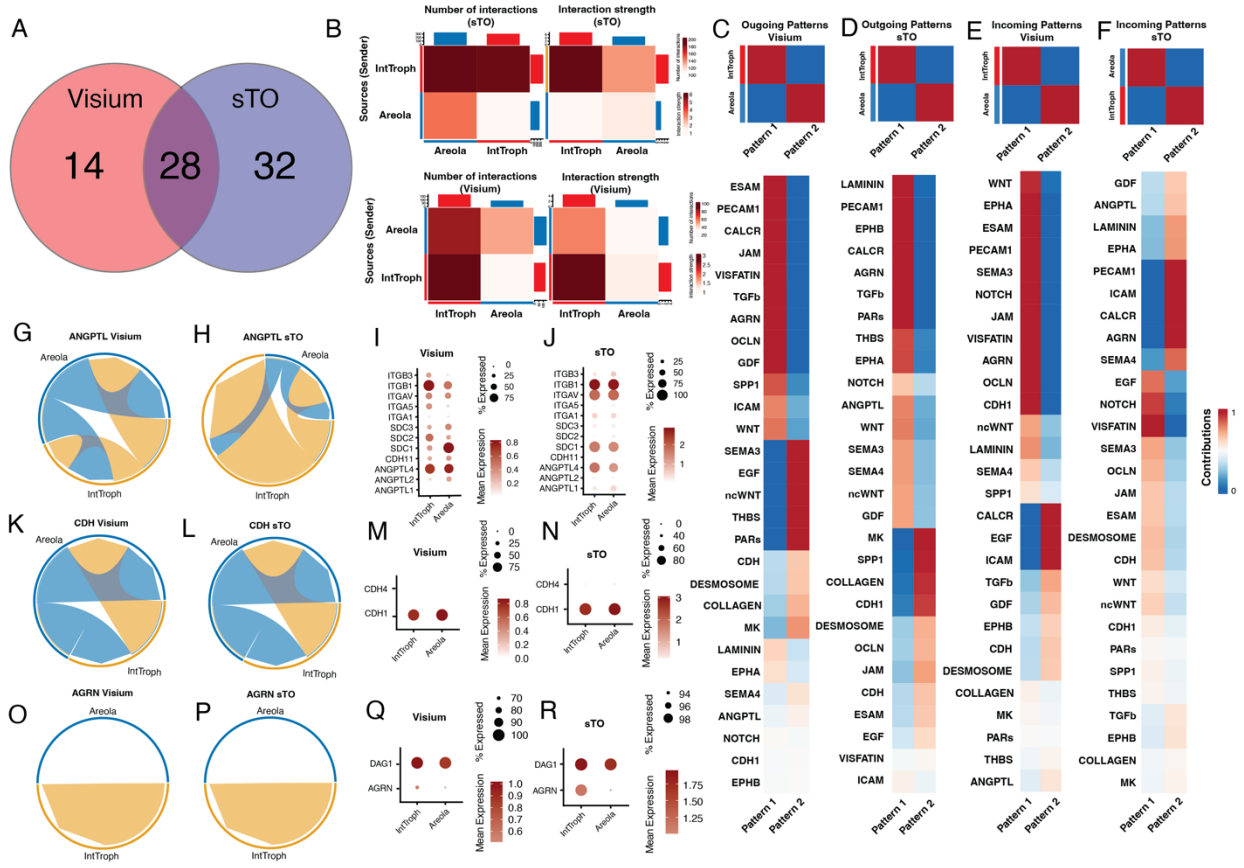

Figure 8: sTOs Recapitulate the Trophoblast Crosstalk Pathways Observed In the Porcine Placenta.
A.) Venn Diagram showing the number of unique and shared trophoblast communication pathways between sTO and porcine trophoblasts *in vivo*. B) Heatmaps showing the number (top left panel) and strength (top right panel) of interactions between clusters within sTO. Similarly, the bottom panels show the number (bottom left panel) and strength (bottom right panel) of interactions within porcine trophoblasts from spatial transcriptomics data. In both cases Color indicates increased number (left) or strength (right) between the sending cluster and the receiving cluster. C-F) Heatmaps showing the signaling patterns (top panels) and the shared signaling pathways contributing to those patterns, for sTO and porcine trophoblasts from spatial transcriptomics. C-D) shows the outgoing patterns for C) porcine trophoblasts obtained via spatial transcriptomics and D) sTO. E-F) shows the incoming patterns for E) porcine trophoblasts obtained via spatial transcriptomics and F) sTO. For upper panels, coloring indicates relative cluster contribution to a pattern with red being high and blue being low contribution level. For lower panels, color indicates the relative contribution of a pathway to a given pattern. G-H) Chord diagrams showing ANGPTL signaling within both G) Visium trophoblasts and H) sTO. I-J) Dotplots showing the expression level of pathways within the ANGPTL pathway for I) Visium trophoblasts and J) sTO. Color of dots denote average expression, whereas size represents percentage of cells in a cluster expressing the gene of interest. K-L) Chord diagrams showing AGRN signaling within both K) Visium trophoblasts and L) sTO. M-N) Dotplots showing the expression level of pathways within the AGRN pathway for M) Visium trophoblasts and N) sTO. Color of dots denote average expression, whereas size represents percentage of cells in a cluster expressing the gene of interest. O-P) Chord diagrams showing CDH signaling within both O) Visium trophoblasts and P) sTO. Q-R) Dotplots showing the expression level of pathways within the CDH pathway for Q) Visium trophoblasts and R) sTO. Color of dots denote average expression, whereas size represents percentage of cells in a cluster expressing the gene of interest.

DISCUSSION

US agricultural commodities from swine account for approximately $62 billion in added economic value and is heavily reliant on successful animal husbandry[46]. In all eutherian mammals, including swine, successful placentation is critical for fetal growth and survival[7]. Therefore, understanding non-human placental function, development, and defenses is critical for ensuring continued reproductive success. While there is growing interest in studying non-human placentation, the lack of appropriate models remains a major hurdle. We and others have demonstrated that trophoblast organoids derived from human placentae are a critical tool for the study of human placentation due to their ability to be passaged, cryopreserved, and to recapitulate human trophoblast heterogeneity[32,34,47]. Here, we report the establishment of swine trophoblast organoids (sTOs), which recapitulate key aspects of the swine placenta.

590 We show that sTOs can be derived from full-term swine placentae, enabling model
591 establishment without the need to sacrifice animals. Like hTOs, sTO can be expanded,
592 cryopreserved, and successfully recovered, making them an ideal *in vitro* model. Current models,
593 such as PTr2 cells, contain a unique expressional profile to swine placental tissue, and express
594 low levels of several trophoblast markers. We show here that sTOs express high levels of the
595 trophoblast markers KRT18, ELF3, and GATA3, and an expressional signature more consistent
596 with swine placentae. Importantly, sTOs cultured within Matrigel spontaneously form an interiorly
597 localized apical surface that is reversible by culturing in suspension, thereby allowing for
598 customization of this model. Together, our data suggest that sTOs better recapitulate the
599 transcriptional signature of swine placental tissue than currently available *in vitro* models.

600 As discussed previously, the swine placenta is distinct from the human placenta at both a
601 structural and cellular level[7]. In humans, placental trophoblasts fall into several distinct
602 subpopulations including CTBs, EVTs, and the STB, all of which have distinct roles in the
603 formation of the hemochorial placenta[7]. In the epitheliochorial placenta, such as those found in
604 swine, there is no direct contact between maternal blood and fetal trophoblasts, which
605 theoretically could limit the efficiency and molecular breadth of nutrient transfer to the developing
606 fetus[7,8]. To facilitate this exchange, the highly folded interface expresses various nutrient
607 transporters and aquaporins[20,21]. Further, the porcine placenta contains a specialized structure
608 known as an areola, which is a dome like cluster of trophoblasts that sit atop uterine glands[22].
609 These structures, which have a peak density of approximately 2500 per placenta[48], collect and
610 transfer maternally-derived histotroph to the fetus as a nutrient source. Indeed, previous studies
611 have indicated that areola surface area is directly correlated with fetal growth, further supporting
612 their critical role in nutrient acquisition[48]. Interestingly, areola structures have been noted in many
613 ungulates, including hippopotamuses[49], dolphins[50], and llamas[51], suggesting that areola are
614 critical for fetal growth across species.

615 Several studies have indicated that these porcine trophoblast subpopulations have some
616 degree of cellular heterogeneity *in vivo.* It is known that along placental folds of the interface,
617 expression of various transporters varies. For example, GLUT1 and GLUT8 have opposing
618 expression profiles, with GLUT1 being located at the base of the folds and GLUT8 being localized
619 to the tip of the folds[40]. Similar spatially localized gene expression has been observed for
620 aquaporins[20]. Additionally, trophoblasts localized to the areola have increased expression of
621 CTSL, AQP5, and ITGB3 relative to other trophoblast populations[20,24,41]. Furthermore, how these
622 various populations differentiate and develop is largely unknown, primarily due to the lack of an
623 *in vitro* model that provides this cellular heterogeneity without the need to consistently access
624 fresh tissue.

625 We and others have previously demonstrated that in human trophoblast organoids, there
626 is extensive cellular heterogeneity, indicating that trophoblast organoids spontaneously
627 differentiate into the various trophoblast populations of the placenta[32-34,52]. Single cell RNA-
628 sequencing of sTO revealed similar cellular heterogeneity within this organoid model. While
629 previous studies have identified markers of various trophoblast subpopulations in swine
630 placentae[20,24,40], these markers were insufficient to segregate sTO cell populations. Using Visium
631 spatial transcriptomics of mid-gestation swine maternal-fetal interfaces, we defined the
632 transcriptomic landscape of swine trophoblast populations *in situ*. By coupling a single cell
633 RNASeq dataset from sTOs and Visium spatial transcriptomics dataset from swine placentae, we
634 were able to assign identities to sTOs populations using an unbiased probabilistic modeling
635 approach. Simultaneously, we identified a shared gene expression profile between sTO cell
636 populations and their corresponding placental cell populations. Using this approach, we
637 demonstrate that sTOs contain a proliferative stem cell population, an interface trophoblast
638 population and three areola trophoblast populations. Critically, this approach allowed for robust
639 identification of cell populations in an unbiased manner.

640 Using trajectory analysis, we defined how sTOs gain their heterogeneity. Using Slingshot,
641 we demonstrate that proliferative stem cells differentiate into interface trophoblasts, which can
642 then differentiate into areola-2 trophoblasts. This analysis uncovered numerous expression
643 changes throughout the differentiation process, including novel targets like ITM2C and NUPR1,
644 which could be investigated in future mechanistic studies to enhance our understanding of swine
645 placental development. Having defined the expressional changes along this trajectory, we then
646 confirmed their localization in tissue finding high concordance between sTOs and tissue level
647 expression, suggesting a shared trajectory between these two systems. By comparing global
648 gene expression changes in sTO derived interface trophoblasts and areola-2 trophoblasts we go
649 on to show that these two populations display starkly different functional niches, with interface
650 trophoblasts being primed to form focal adhesions and promote angiogenesis, whereas areola-2
651 trophoblasts were enriched in programs for the formation of endosomes. It is noted within the
652 literature that areola trophoblasts contain a high number of intracellular vesicles, presumably to
653 facilitate transport of histotroph across this epithelial barrier[22]. As expected, when we examined
654 the expression of key endosome markers within the tissue and sTO, we observed similar patterns
655 of expression, with endosome markers expressed at a higher level in areola-2 cells compared to
656 interface trophoblasts. Together, these data demonstrate that sTOs recapitulate the
657 developmental and functional differences in trophoblast populations observed in the porcine
658 placenta, highlighting their utility in studying porcine placental development.

659 While combining sTO and spatial datasets allowed for robust cell cluster identification,
660 parallel analyses enabled us to further explore the functional similarities between sTOs and
661 placental tissue. Using CellChat, we first identified dozens of signaling pathways occurring at the
662 porcine maternal-fetal interface. Interestingly, we found several instances of inter-trophoblast
663 signaling within the porcine placenta. By applying CellChat to the shared trophoblast populations
664 found within our sTO and placental tissue datasets, we revealed several key signaling pathways
665 are conserved between these systems. For example, we that the angiopoietin-like proteins

666 (ANGPTL), Agrin (AGRN), and Cadherin (CDH) pathways are highly conserved within sTO and
667 tissue trophoblasts. These pathways have been shown to be active in the placenta and play
668 important roles in regulating epithelial to mesenchymal transitions, basement membrane function,
669 and nutrient metabolism [53-56]. Importantly, sTO recapitulated autocrine and paracrine signaling
670 patterns observed in placental tissue, highlighting their utility as a physiologic model. Importantly,
671 these analyses were based on known human receptor-ligand interactions and rely on shared
672 annotations between the human and porcine genome. It remains possible that some receptor-
673 ligand pairs in the porcine genome are not annotated, which would preclude them from being
674 included as an interaction in our results. Therefore, this represents a conservative estimate of
675 cell-cell communication in the porcine placenta. We believe that these data provide a robust
676 framework for hypothesis generation for understanding signaling within the porcine placenta.

677 Previous studies have used single cell RNA-sequencing to characterize the porcine uterus
678 and embryos[25,26,45,57]. However, these studies rely on existing markers or GO-term based
679 functions to assign cellular identity, lack histological structural context, do not provide spatial
680 segregation of gene expression signatures, and were not performed at a gestational stage where
681 critical structures, such as the areola, are present. Our data robustly define the expression profiles
682 of various histological structures at the swine maternal-fetal interface. By mapping gene
683 expressions directly to corresponding histological structures, we confirmed cellular identities
684 without relying on conventional markers, making this assignment unbiased. Moreover, using mid-
685 gestation swine maternal-fetal interfaces, we were able to characterize the expression profiles of
686 key structures, including the areola and the interface, which have previously eluded detailed
687 analyses. This dataset provides new insights into placental biology that were not achievable with
688 earlier approaches.

689 Demonstrating the utility of this spatially resolved dataset, we identified two
690 transcriptionally and structurally distinct areola populations within the porcine placenta: Areola-2,
691 which appears continuous with the interface trophoblasts, and Areola-1, which is localized

692 primarily to the placental interstitium without evidence of direct contact with the interface. This
693 finding emphasizes the power of spatial transcriptomics in revealing previously unrecognized
694 cellular diversity within structurally complex tissues such as the placenta. While both clusters
695 expressed high levels of the known areola marker CTSL[24], these clusters had divergent gene
696 expression profiles with Areola-2 expressing high levels of MDK, CTSD, PAG2L2 and Areola-1
697 expressing high levels of CCDC162, SPINK4, and MMP25. While it remains unclear why these
698 two areola populations exist, previous results[24] have shown that histologically similar CTSL
699 positive structures exist within the porcine placenta. It is possible that these represent areola at
700 different stages of development, with Areola-1 representing a more mature population due to its
701 higher expression of CTSL and its increased size. Together, these findings highlight the power
702 and utility of the spatial transcriptomic dataset in advancing our understanding of the fundamental
703 biology of the porcine placenta.

704 Our work offers a comprehensive characterization of spatial gene expression in the
705 porcine placenta and successfully establishes an organoid model that captures its cellular
706 heterogeneity. However, limitations include the resolution of Visium spatial transcriptomics, which
707 does not allow for single-cell level definition of histological populations. For example, the identified
708 Visium clusters may represent a mixture of gene expression profiles but nonetheless captures
709 the dominant signals of key structures and cell populations. For instance, although we observed
710 some overlap in marker expression between uterine epithelium and trophoblast populations,
711 these clusters still separate along the interface. Moreover, the populations are strongly
712 represented by known markers, indicating that despite resolution constraints, this technique
713 effectively segregates distinct populations and provides robust biological insights. Another
714 limitation of this study is that we focused on a single mid-gestation timepoint. While this provides
715 valuable insights into the biology of the porcine placenta during this stage, it limits our ability to
716 assess dynamic changes in cellular composition and signaling across different stages of
717 gestation. While previous studies have highlighted that human trophoblast organoids represent

718 first trimester tissue[33,35], our bulk RNA-seq data demonstrated that sTOs have similar expression
719 to porcine placentae regardless of gestation. It remains possible that early or later gestation
720 placentae would have mapped with higher probabilities to sTO populations enabling more robust
721 identification. Future studies aimed at capturing multiple gestational timepoints in the porcine
722 placenta are therefore warranted. While the data presented here demonstrate the utility and
723 strength of spatial transcriptomics, they represent only a portion of the insights generated in this
724 study. The thousands of spatially resolved genes and pathways identified provide a valuable
725 resource for advancing porcine reproductive biology. To facilitate broader access, we have
726 developed a user-friendly web-based app, enabling researchers without advanced computational
727 resources to explore and analyze the data (see data availability statement for further details)

728 We believe this study serves as a foundational study for studying the porcine placenta, via
729 the presentation of a physiologic model and a spatially resolved roadmap of the maternal-fetal
730 interface. These critical findings allow for future studies to be proposed. For example, future
731 studies aimed at studying the function of the signaling pathways identified here may discover new
732 avenues to reduce reproductive failure, including failure caused by vertical transmission of
733 pathogens or defective placentation. Additionally, these data may inform studies aimed at
734 identifying the triggers of areola development, which may now be possible *in vitro.* We hope that
735 these data will spark new interest in studying porcine reproductive biology.

736 Taken together, our study describes the derivation of an organoid model that recapitulates
737 the cellular heterogeneity and functionality of the swine placenta. Additionally, we provide a
738 spatially resolved expression landscape of the swine maternal-fetal interface, creating a valuable
739 resource for the study of non-human placentation. The ability to map gene expression directly to
740 histological structures offers unprecedented insights into the cellular dynamics of the porcine
741 placenta, setting a new benchmark for comparative placental biology research. These findings
742 have the potential to significantly advance our understanding of placental biology across
743 eutherians, offering a critical framework for studying key aspects of maternal-fetal communication

744 and placental development. Moreover, the organoid model and spatial transcriptomic data will
745 serve as foundational tools for exploring mechanisms of placental function and dysfunction, with
746 broader implications for reproductive biology and veterinary medicine.
747

748 **METHODS**

749 **Animal Husbandry and Tissue Collection**

750 *Tissue Collection for sTO Derivation*

751 Placentae for swine trophoblast organoids (sTO) were collected from crossbred sows consisting
752 of Yorkshire, Large White, and Landrace breeds from the North Carolina State University (NCSU)
753 Swine Educational Unit (SEU), which is a facility free from Porcine Reproductive and Respiratory
754 syndrome virus (PRRSV), swine influenza A virus and mycoplasma species. The average
755 gestation length of sows at the SEU is 114.2 +/- 1.3 days. At SEU older parity sows (n = 2; parity
756 5) that didn't farrow by 114 days were induced using 2mL of Lutalyse (Dinoprost tromethamine
757 injection, Zoetis) intramuscularly, whereas gilts (n=1) were allowed to farrow naturally. Placentae
758 collected from gilts or sows were placedin ziploc bags containing Dulbecco's Modified Eagle
759 Medium (DMEM, Cytiva Hyclone cat. # SH30081.01) supplemented with 10% inactivated fetal
760 bovine serum (FBS, Biowest #S1620 Heat Inactivated, USDA approved origin), 1100 IU/mL
761 penicillin, 1100 mg/mL streptomycin (Cytiva Hyclone 100x solution, #SV30010), 2 mM L-
762 glutamine (GIBCO 100x 200mM, #A2916801), Amphotericin B 2.5 µg/ml (Gibco, Fungizone,
763 15290-018)). Placentae were collected under experimental procedures approved by the NCSU
764 Institutional Animal Care and Use Committee (IACUC) ID# 22-122-B (n=2, gilts, IM Lutalyse
765 injection) or via normal farrowing activities performed in NCSU SEU (n=3))
766

767 *Tissue Collection for Visium Spatial Transcriptomics*

768 Animal procedures carried out in compliance with Purdue University's animal care policies and
769 approved by the Institutional Animal Care and Use Committee (IACUC Protocol #2104002130),

770 and as previously described [58]. In short, a total of n=3 commercial landrace/large white composite
771 gilts, were selected from the Animal Sciences Research and Education Center (ASREC) at
772 Purdue University, synchronized with oral progestogen (Altrenogest at 17.6 mg/day for 14 days).
773 Following withdrawal, the gilts were heat checked twice daily with an intact boar, and artificially
774 inseminated 12 hours after the first observed lordosis responses, and every 24 hrs there after
775 until the end of estrus. Pregnancy was confirmed via transcutaneous ultrasound on gestation day
776 30-35. Gilts were fed a standard gestation diet comprised of corn, soybean meal and dried
777 distillers grain, and formulated to meet the dietary requirements as outlined by the NCR. On
778 gestation day 65 (relative to first artificial insemination) pregnant gilts were stunned with a
779 penetrating captive bolt and euthanized via rapid exsanguination. The gravid uterus carefully
780 extracted though a midline incision and linearized such that each fetus and its corresponding
781 placenta could be isolated. Sections of the maternal fetal interface were collected adjacent to the
782 umbilical stump and a roughly 1 cm^2 section of intact placenta (maternal and fetal tissue) was
783 excised, embedded in optimal cutting temperature media (OCT) (Tissue-Plus OCT Compound;
784 Fisher Scientific) and slowly cooled to cryogenic temperature using dry ice.
785

786 **Derivation, culture, and passaging of sTO**

787 sTOs were derived using a previously established method used for the derivation of human
788 trophoblast organoids[33]. Briefly, placentae were extensively rinsed with Phosphate Buffered
789 Saline (PBS) and sequentially digested with 0.2% trypsin-250 (Alfa Aesar, J63993-09)/0.02%
790 EDTA (Sigma-Aldrich, E9884-100G) and 1.0 mg/mL collagenase V (Sigma-Aldrich, C9263-
791 100MG). Digested tissue was then disrupted by pipetting up and down vigorously ~10 times with
792 10 mL serological pipette (VWR, 89130-898; MSP, 62-1005-10) and pooled prior to washing with
793 Advanced DMEM/F12 medium (Life Technologies 12634-010). Pelleted digests were then
794 resuspended in ice-cold growth-factor reduced Matrigel (Corning 356231). Matrigel 'domes'
795 (40 µL/well) were plated into 24-well tissue culture plates (Corning 3526), placed in a 37° C

796 incubator to pre-polymerize for ~3 min, turned upside down to ensure equal distribution of the
797 isolated cells in domes for another 10 min, then overlaid with 500 µL prewarmed term trophoblast
798 organoid medium (tTOM).
799
800 tTOM consisted of Advanced DMEM/ F12 (Life Technologies, 12634-010) supplemented with 1×
801 B27 (Life Technologies, 17504-044), 1× N2 (Life Technologies, 17502-048), 10% fetal bovine
802 serum (FBS) (vol/vol, Cytiva HyClone, SH30070.03), 2 mM GlutaMAX supplement (Life
803 Technologies, 35050-061), 100 µg/mL Primocin (InvivoGen, antpm-1), 1.25 mM N-Acetyl-L-
804 cysteine (Sigma-Aldrich, A9165), 500 nM A83-01 (Tocris, 2939), 1.5 µM CHIR99021 (Tocris,
805 4423), 50 ng/mL recombinant human EGF (Gibco, PHG0314), 80 ng/mL recombinant human R-
806 spondin 1 (R&D systems, 4645-RS-100), 100 ng/mL recombinant human FGF2 (Peprotech, 100-
807 18C), 50 ng/mL recombinant human HGF (Peprotech, 100-39), 10 mM nicotinamide (Sigma-
808 Aldrich, N0636-100G), 5 µM Y-27632 (Sigma-Aldrich, Y0503-1MG), and 2.5 µM prostaglandin E2
809 (PGE2, R&D systems, 22-961-0).
810 Cultures were maintained at 37° C in a humidified incubator with 5% CO2. Medium was
811 renewed every 2–3 days. Small trophoblast organoid spheroids became visible by approximately
812 7-10 days post isolation. Derived sTO were passaged every 5–7 days depending on their size
813 and density. To passage, spent media was removed from sTO and fresh Advanced DMEM/F12
814 added to the well. Domes were disrupted using a pipet tip and pelleted via centrifugation. Pellets
815 were then digested in prewarmed TrypLE Express (Life Technologies, 12605- 028) at 37° C for
816 5–7 min. Pelleted organoids were then further dissociated manually using a P200 pipette by
817 vigorously pipetting approximately 200-300 times. Dissociated sTOs were pelleted and
818 resuspended in fresh ice-cold Matrigel and replated as domes at the desired density for
819 continuous culture. All experiments described in this paper were performed in sTOs under
820 passage 15 to limit potential passage level effects.

821 For cryopreservation, sTOs were grown to high density and spent media was aspirated.
822 CryoStor CS10 (Stem Cell Technologies; # 07930) was then added 1mL per 'dome' and domes
823 disrupted using a p1000 pipette. Organoids were then transferred to a sterile cryovial and
824 gradually frozen to -80°C using a CoolCell (Corning). After 24 hours vials were transferred to
825 vapor phase liquid nitrogen for long term storage. To thaw cryopreserved organoids, cryovials
826 were rapidly thawed (<2min) in a 37°C water bath with gentle agitation. Freezing media and
827 organoids were then transferred to a 15mL conical and resuspended 9mL of prewarmed
828 Advanced DMEM/F12. Organoids were then pelleted and resuspended in ice cold Matrigel and
829 seeded into 'domes' in 24 well plates. Fresh tTOM including 5 μM Y-27632 (Sigma-Aldrich,
830 Y0503-1MG) was added prior to incubation for 24-72 hours at 37°C with 5% CO_2. sTO were then
831 passaged as described above.
832
833 **Reversal of sTO Polarity**
834 To reverse organoid polarity, we utilized a previously established protocol we developed to invert
835 hTOs[32]. Briefly, spent media was removed and 1mL of ice-cold cell recovery media (Corning Cat#)
836 added to each well. Domes were gently disrupted using a P1000 and organoids transferred to a
837 15mL conical. Organoids were incubated for 30 minutes on ice to dissolve Matrigel prior to being
838 washed twice using 1x DPBS. Organoids were then resuspended in 500mL of prewarmed TOM
839 and plated into ultra-low binding 24 well plates. Organoids were incubated statically at 37°C with
840 5% CO_2 for 48 hours prior to usage.
841
842 **Histology and Immunofluorescence Staining of sTOs**
843 Mature organoids were fixed using 4% paraformaldehyde in PBS for 15 minutes and subsequently
844 washed with PBS. Histology was performed by HistoWiz Inc. (histowiz.com) using a Standard
845 Operating Procedure and fully automated workflow. Samples were processed, sectioned at 5μm.

846 Whole slide scanning (40x) was performed on an Aperio AT2 (Leica Biosystems). For
847 immunofluorescence staining, whole mount staining of organoids was performed using previously
848 described methods with some modifications. Briefly, organoids were removed from PBS and
849 permeabilized for 10 minutes in a permeabilization buffer consisting of 0.5% Triton X-100 and 1%
850 Bovine Serum Albumin (BSA) in PBS. Organoids were then pelleted and stained overnight using
851 a ZO-1 antibody conjugated to AlexaFluor 488 (Santa Cruz) at a dilution of 1:50 in
852 permeabilization buffer. The organoids were then pelleted and washed twice in PBS, prior to
853 staining with Phalloidin conjugated to AlexaFluor 633 (Thermo) according to manufacturer's
854 instructions. Organoids were then pelleted and washed twice in PBS prior to mounting with
855 Vectashield containing DAPI. Slides were then imaged using Olympus Fluoview FV3000 inverted
856 confocal microscope and images processed using FIJI. Brightfield images of whole organoids
857 were obtained from fresh, mature, unfixed wells using a Keyence BZ-X810 all-in-one fluorescence
858 microscope
859
860 **Bulk RNA-Sequencing of sTO**
861 *RNA Isolation, Library Prep, and Sequencing*
862 Total RNA was isolated with the Sigma GenElute total mammalian RNA miniprep kit (Cat #
863 RTN350-1KT) or Qiagen RNAeasy Mini Kit (Cat #74104) following the manufacturer's instruction
864 and using supplementary Sigma DNase digestion. RNA quality and concentration were
865 determined using a Nanodrop ND-1000 Spectrophotometer. For bulk RNA-seq analysis, RNA
866 was isolated from organoids as described above. Purified Total RNA was verified by Thermo
867 scientific Nanodrop one. The libraries were prepared by the Duke Center for Genomic and
868 Computational Biology (GCB) using the Tru-Seq stranded total RNA prep kit (Illumina).
869 Sequencing was performed on the NovaSeq 500 by using 75-bp paired-end sequencing.
870

871 For PTr2 cells, raw reads from a previously published study were downloaded from the Sequence
872 Read Archive (SRA): SRR16912824, SRR16912825, and SRR16912827. Similarly, raw reads for
873 GD60, GD90, and L0 tissues were downloaded from SRA: SRR6703668, SRR6703669,
874 SRR6703670, SRR6703671, SRR6703672, SRR6703673, SRR6703674, SRR6703675,
875 SRR6703676, and SRR6703677.
876
877 *Bulk RNA-seq Analysis*
878 Raw reads were aligned to the swine genome (susScr11) using QIAGEN CLC Genomics (v20)
879 and mapped data were exported and compiled. The packages tidyverse, magrittr, pheatmap, rio,
880 factoextra, ggforce, tidyheatmap, and DESeq2 were utilized for analysis. All analyses were
881 performed using package specified methods. Heatmaps were made using pheatmap and
882 tidyheatmap, with row scaling and hierarchical clustering of both rows and columns. For sex
883 determination analyses an established protocol for sexing pigs using bulk rna-sequencing data
884 was utilized, with minor modifications [39]. Briefly, the summation of the following 9 Y-linked genes:
885 EIF2S3Y, ZFY, KDM5D, EIF1AY, DDX3Y, LOC100625207, LOC110257894, LOC110255257,
886 and LOC110255320. Summation scores below 2 are considered female, whereas scores above
887 2 are considered male.
888
889 **Single-Cell RNA-Sequencing of sTOs**
890 sTO from three independent lines (STO01, STO02, and STO04) were grown to high density using
891 the method above. Spent media was removed from the wells and fresh Advanced DMEM/F12
892 added to the well. Domes were disrupted using a pipet tip and pelleted via centrifugation. Pellets
893 were then digested in prewarmed TrypLE Express (Life Technologies, 12605- 028) at 37° C for
894 10-15 min. Pelleted, digested organoids were then further dissociated using a 23G needle
895 aspirating and ejecting 3 times. For STO01 and STO04 a dead cell removal step was performed
896 (Miltenyi Biotech catalog #: 130-090-101) per manufacturer's instructions. Disassociated sTO

897 were then filtered through a 40um cell strainer, which was subsequently washed using 4mL of
898 Advanced DMEM/F12. Pelleted cells were then resuspended in fresh Advanced DMEM/F12 and
899 placed on ice until viability counts were performed.
900
901 Libraries were prepared following standard 10x Genomics Single Cell Gene Expression 3'
902 protocols. Samples containing highly viable cells (80% viability or higher), were washed and
903 filtered through 40μm filter and resuspended in a 1x PBS / 0.04% BSA buffer, at a concentration
904 of 1000 cells/μL. A Cellometer K2 instrument (Nexcelom - Lawrence, MA) was then used to
905 determine the concentration of the single cell suspension. Cells were then suspended in master
906 mix containing reverse transcription (RT) reagents using a volume equivalent to the target capture
907 number of 10,000 cells (plus approximately 60% overage to account for capture efficiency of the
908 assay). This master mix was loaded onto the 10x microfluidics chip, together with gel beads
909 carrying the Illumina TruSeq Read 1 sequencing primer, a 16bp 10x barcode, a 12bp unique
910 molecular identifier (UMI) and a poly-dT primer, and oil for the emulsion reaction. The Chromium
911 X instrument was then used to generate gel beads in emulsion (GEMS) for the RT and barcoding
912 of single cells. After the RT reaction, the GEMs were broken, full length cDNAs were cleaned with
913 Silane Dynabeads, and then amplified via PCR. Following purification using SPRI bead size
914 selection the cDNAs were assayed on a 4200 TapeStation 4200 High Sensitivity D5000
915 ScreenTape (Agilent - Santa Clara, CA) for qualitative and quantitative analysis.
916
917 Enzymatic fragmentation and size selection were used to optimize the cDNA amplicon size for
918 the sequencing library preparation in which Illumina P5 and P7 sequences (San Diego, CA), a
919 sample index, and TruSeq read 2 primer sequence are added via end repair, A-tailing, adaptor
920 ligation, and PCR. The final libraries contained P5 and P7 primers used in Illumina bridge
921 amplification. Following additional purification libraries were assayed for quality, using a
922 TapeStation HSD1000 ScreenTape, then quantitated and checked for successful adapter ligation

923 with the KAPA Library Quantification Kit (Roche-Indianapolis, IN). Sequences were generated
924 using paired end sequencing on an NovaSeq X Plus, at ~62k reads/cell.
925
926 **Analysis of Single Cell Data**
927 *QC and Cluster Analysis*
928 FASTQ files were uploaded to the 10X Cloud Analysis website
929 (https://www.10xgenomics.com/products/cloud-analysis) and analyzed using cellranger v7.1.0
930 using Sus scrofa genome v11.1 downloaded from Ensembl (www.ensembl.org). Mapped files
931 were downloaded through command line and filtered feature matrices utilized for secondary
932 analyses in R using a Seurat based pipeline [59]. Briefly, the packages Seurat v4.4.0, SeuratObject
933 v5.0.1, and SeuratWrappers v0.2.0, devtools 2.4.5, dplyr v1.1.4, harmony v1.2.0, and patchwork
934 v1.2.0, were used for analysis. Individual imported filtered feature matrices underwent filtering for
935 to only include cells with nFeatures falling between 2500-15000, nCounts lower than 200,000,
936 percent mitochondrial reads falling between 0.05-1, and percent ribosomal reads lower than 3.
937 Matrices were then merged, and individually normalized using SCTransform, regressing percent
938 mitochondrial reads, percent ribosomal reads, nFeatures, and nCounts. Integration of the data
939 was then performed on the SCT normalized data using SelectIntegrationFeatures (nFeatures =
940 4000), PrepSCTIntegration, FindIntegrationAnchors, and the IntegrateData commands.
941 Dimensional reduction using RunPCA and RunUMAP was then performed using the top 30
942 dimensions, followed by cluster analysis (FindNeighbors and FindClusters) at a resolution of 0.2.
943 This resolution was selected because it was able to clearly resolve clusters by markers, with
944 minimal overlap in markers between clusters, and to optimize probabilistic mapping to tissue in
945 downstream analyses. Prior to subsequent analyses, where indicated, the RNA assay was
946 normalized and scaled (NormalizeData and ScaleData, and ALRA (RunALRA) mediated
947 imputation of the data was performed as previously described. Marker identification was
948 performed using the FindAllMarkers function using the ALRA assay, with a minimum fold change

threshold of 0.25 and detected in a minimum of 0.25 of cells. For marker analyses the default Seurat adjusted p-value of $p < 0.01$ (Bonferroni correction) was considered significant.

Pseudotime Analysis

The differentiation trajectories from Seurat-identified clusters were determined using the Slingshot package (version 2.6.0) in R [60]. The root was set at the proliferative trophoblasts, which expressed the highest levels of stemness markers, and allowed inference of downstream differentiation paths without further constraint. The raw RNA count data and the generated Slingshot object were then utilized to run the evaluateK() function, testing a range of 3 to 9 knots. The optimal number of knots was determined to be 4. Subsequently, the fitGAM() function in tradeSeq (version 1.5.10) was applied using this optimal value, and lineage-specific gene expression was identified through the associationTest() function[61]. Heatmaps of expression changes along the lineages were created using ComplexHeatmap() on log-transformed counts, and were rasterized using the "Bessel" filter in ImageMagick[62]. Finally, the plotGenePseudotime() function was used to visualize raw count gene expression across individual cells along the lineages derived from the Slingshot object.

Differential Expression and GO-Term Analysis

To perform differential expression between clusters, the FindMarkers function was utilized setting the LogFoldChange threshold to 0.01. Significant hits were defined as having a Log2FoldChange of at least 0.25 and an adjusted p-value < 0.01 (Bonferroni correction). GO-Term was performed using DAVID pathway analysis Significant hits were then input into the Database for Annotation, Visualization and Integrated Discovery (DAVID; https://david.ncifcrf.gov/home.jsp) and GO-Terms exported. Significantly enriched GO-Terms were defined as GO-Terms with a p-value <0.05 after Bonferroni correction.

975 *CellChat Analysis for sTOs*

976 Cellchat for sTO were performed using previously established methods[63,64]. Briefly, interaction
977 inputs, complex inputs, cofactor inputs, and gene info inputs were downloaded from CellChatDB
978 and cellchat objects were created using the ALRA assay. Overexpressed genes and interactions
979 were then identified using the identifyOverExpressedGenes and
980 identifyOverExpressedInteractions functions and gene expression projected onto a protein-
981 protein network using projectData. Communication probabilities were then calculated using the
982 computeCommunProb function. Communications were then filtered to include interactions
983 including a minimum of 10 cells (filtercommunication function) and probabilities calculated using
984 computeCommunProbPathway function. Aggregated networks were then calculated using
985 aggregateNet and centrality calculated using netAnalysis_computeCentrality function. Patterning
986 analysis was performed first by selecting a number of patterns using the selectK function, which
987 was assigned based on when the which Cophenetic and Silhouette values droped suddenly.
988 Pattern plots were generated using the identifyCommunicationPatterns function. Additional plots
989 were generated using standard methods as described in detailed scripts.

990

991 **Spatial Transcriptomics of Mid-Gestation Pig Placentae**

992 Tissues embedded in optimal cutting temperature (OCT) compound were sectioned at 10 μm
993 thickness and placed on a Tissue Optimization (TO) Slide to determine optimal permeabilization
994 conditions. After establishing the conditions, tissue sections were positioned within a 6.5 mm^2
995 capture area on an expression slide containing 5,000 spatially barcoded probes. The tissues were
996 subsequently fixed and stained with Hematoxylin and Eosin. Following staining, the tissues were
997 permeabilized to release mRNA, which hybridized to the spatially barcoded capture probes,
998 enabling the capture of gene expression data. Barcoded cDNA was synthesized on the slide from
999 the captured mRNA, denatured, cleaved, and transferred into a PCR tube for amplification. The
1000 amplified cDNA was then used to generate standard next-generation sequencing (NGS) libraries.

1001 In brief, the amplified cDNA was enzymatically fragmented, purified, and size-selected.
1002 Sequencing adapters were ligated to each fragment, followed by sample index PCR. The resulting
1003 libraries were sequenced on a NovaSeq6000 SP flow cell with an average of 50,000 reads per
1004 probe, using a 28x10x10x90 read format.
1005

1006 **Analysis of Visium Data**

1007 *QC and Cluster Analysis*

1008 FASTQ files were analyzed using Spaceranger v2.1.1 using Sus scrofa genome v11.1
1009 downloaded from Ensembl (www.ensembl.org). Filtered feature matrices were then utilized for
1010 secondary analyses in R using a Seurat based pipeline [59]. Briefly, the packages Seurat v4.4.0,
1011 SeuratObject v5.0.1, and SeuratWrappers v0.2.0, devtools 2.4.5, dplyr v1.1.4, harmony v1.2.0
1012 and patchwork v1.2.0 were used for analysis. Individual imported filtered feature matrices
1013 underwent filtering for to only include cells with nFeatures falling above 200 and percent ribosomal
1014 reads lower than 20. Matrices were then merged, and individually normalized using SCTransform,
1015 regressing percent ribosomal reads, nFeatures, and nCounts. Variable features across the
1016 datasets were then obtained using SelectIntegrationFeatures and datasets were remerged using
1017 Merge_Seurat_List. Variable features were then set using VariableFeatures and dimensional
1018 reduction and cluster analysis performed using RunPCA on the top 50 dimensions. Cluster
1019 analysis was then perfomed using FindNeighbors (top 30 dimensions), FindClusters (resolution
1020 of 0.3), and RunUMAP (top 30 dimensions). Prior to subsequent analyses, where indicated, ALRA
1021 (RunALRA) mediated imputation of the data was performed as previously described. Marker
1022 identification was performed using the FindAllMarkers function using the ALRA assay, with a
1023 minimum fold change threshold of 0.25 and detected in a minimum of 0.25 of cells. For marker
1024 analyses the default Seurat adjusted p-value of $p < 0.01$ (Bonferroni correction) was considered
1025 significant.
1026

1027 *Probabilistic Modeling Based Identification of sTO Clusters*

1028 To identify the cluster identities in sTO we utilized a previously established method to map single
1029 cell data to visium spatial transcriptomics data [59,65]. Briefly, visium spatial transcriptomics data
1030 were first subsetted to only include structures known to contain trophoblasts, which reduces non-
1031 specific signal. Visium data were then set to the SCT data, whereas sTO single cell data were set
1032 to the integrated assay. Probabilistic transfer of labels was then performed using
1033 FindTransferAnchors and TransferData functions, using sTO data as a reference and subsetted
1034 visium data as the query. To identify shared markers between sTO and their corresponding tissue
1035 structures, marker lists for the SCT assay of sTO and the SCT assay of the visium data were
1036 generated using FindAllMarkers with a minimum fold change threshold of 0.25 and detected in a
1037 minimum of 0.25 of cells, with adjusted p-values of 0.01 considered significant. Individual sTO
1038 clusters and their corresponding tissue structure clusters were then filtered and the lists inner
1039 joined to generate shared marker lists.

1040

1041 *CellChat Analysis for Visium*

1042 Cellchat was performed using previously established methods using the packages CellChat and
1043 NMF [63,64]. Briefly, interaction inputs, complex inputs, cofactor inputs, and gene info inputs were
1044 downloaded from CellChatDB and cellchat objects were created using the ALRA assay.
1045 Overexpressed genes and interactions were then identified using the
1046 identifyOverExpressedGenes and identifyOverExpressedInteractions functions. Communication
1047 probabilities were then calculated using the computeCommunProb function. Interactions were
1048 corrected for both distance and cell to cell contact, with the maximum diffusion
1049 interaction/diffusion length being set to 250μm and the cell spot center to spot center range being
1050 set to 100μm. Communications were then filtered to include interactions including a minimum of
1051 10 cells (filtercommunication function) and probabilities calculated using

computeCommunProbPathway function. Aggregated networks were then calculated using aggregateNet. Patterning analysis was performed first by selecting a number of patterns using the selectK function, which was assigned based on when the which Cophenetic and Silhouette values droped suddenly. Pattern plots were generated using the identifyCommunicationPatterns function. Additional plots were generated using standard methods as described in detailed scripts.

Comparative CellChat Analysis for Visium and Single Cell

Briefly, visium spatial transcriptomics data and sTO single cell datasets were subset to only include areolar trophoblasts and interface trophoblast populations. These populations were then combined into a single areola and interface trophoblast cluster for each dataset. Cellchat was then performed as described for sTO (see above). The only modification for this analysis was the interaction filtering was modified to a minimum of 1 cell to account for rare cell populations. Additionally, for patterning analyses, only pathways found in both datasets are shown. All dotplots shown using the ALRA assay.

DATA AND CODE AVALIABILITY

All code is publicly available on the Coyne Lab Github (https://github.com/CoyneLabDuke/Swine-maternal-fetal-interface). All raw and mapped data obtained via Bulk RNA-Sequencing, Single Cell, and Visium Spatial Transcriptomics data generated in this paper are deposited on the Gene Expression Omnibus (GSE296975) and additionally are available via the Sequencing Read Archive (under bioproject number PRJNA1252046). Additionally, a searchable, user-friendly version of the Visium Spatial Transcriptomics dataset has been uploaded at https://coynelab.shinyapps.io/myshinyapp/.

ACKNOWLEDGEMENTS

We would like to thank the Duke Molecular Genomics Core facility for assistance with the generation of bulk RNA-sequencing data, Single-Cell Transcriptomics data, and Visium Spatial Transcriptomics data.

FUNDING SOURCES

This work was supported by funds from Duke University (C.B.C.). Placental tissues samples were derived from work supported by the Foundational and Applied Science Program, project award no. 2023-67015-39338 (JAP), from the U.S. Department of Agriculture's National Institute of Food and Agriculture. The funders had no role in study design, data collection and analysis, decision to publish, or preparation of the manuscript.

SUPPORTING INFORMATION

Supplemental Figures: Supplemental Figures 1-5

Supplemental Movie 1: 3D image reconstruction of sTO grown in matrigel

Supplemental Movie 2: 3D image reconstruction of sTO grown in suspension

Supplemental Table 1: Single cell marker analysis from sTO

Supplemental Table 2: Visium marker analysis from the porcine maternal-fetal interface

Supplemental Table 3: Shared markers between sTO cluster 0 and Visium interface trophoblasts

Supplemental Table 4: Shared markers between sTO cluster 1 and Visium areola-2 trophoblasts

Supplemental Table 5: Shared markers between sTO cluster 3 and Visium areola-2 trophoblasts

Supplemental Table 6: Shared markers between sTO cluster 4 and Visium areola-1 trophoblasts

Supplemental Table 7: GO-terms enriched in Visium interface-trophoblasts

1102 **Supplemental Table 8: GO-terms enriched in Visium areola-2 trophoblasts**

1103 **Supplemental Table 9: GO-terms enriched in sTO interface-trophoblasts**

1104 **Supplemental Table 10: GO-terms enriched in sTO areola-2 trophoblasts**

1105 **Supplemental Table 11: Gene expression signatures across sTO differentiation identified**

1106 **via Slingshot**

1107

1108

1109

1110

1111

1112

1113

1114

1115

1116

1117

1118

1119

1120

1121

1122

1123

1124

1125

1126

1127

1128

1129 **BIBLIOGRAPHY**

1130 1. Hay, W.W., Jr. (1994). Placental transport of nutrients to the fetus. Horm Res *42*, 215-
1131 222. 10.1159/000184196.

1132 2. Lager, S., and Powell, T.L. (2012). Regulation of nutrient transport across the placenta. J
1133 Pregnancy *2012*, 179827. 10.1155/2012/179827.

1134 3. Tal, R., and Taylor, H.S. (2000). Endocrinology of Pregnancy. In Endotext, K.R.
1135 Feingold, B. Anawalt, M.R. Blackman, A. Boyce, G. Chrousos, E. Corpas, W.W. de
1136 Herder, K. Dhatariya, K. Dungan, J. Hofland, et al., eds.

1137 4. Arora, N., Sadovsky, Y., Dermody, T.S., and Coyne, C.B. (2017). Microbial Vertical
1138 Transmission during Human Pregnancy. Cell Host Microbe *21*, 561-567.
1139 10.1016/j.chom.2017.04.007.

1140 5. Megli, C.J., and Coyne, C.B. (2022). Infections at the maternal-fetal interface: an
1141 overview of pathogenesis and defence. Nat Rev Microbiol *20*, 67-82. 10.1038/s41579-
1142 021-00610-y.

1143 6. Roberts, R.M., Green, J.A., and Schulz, L.C. (2016). The evolution of the placenta.
1144 Reproduction *152*, R179-R189. 10.1530/Rep-16-0325.

1145 7. Moffett, A., and Loke, C. (2006). Immunology of placentation in eutherian mammals. Nat
1146 Rev Immunol *6*, 584-594. 10.1038/nri1897.

1147 8. Mika, K., Whittington, C.M., McAllan, B.M., and Lynch, V.J. (2022). Gene expression
1148 phylogenies and ancestral transcriptome reconstruction resolves major transitions in the
1149 origins of pregnancy. Elife *11*. 10.7554/eLife.74297.

1150 9. Carter, A.M. (2012). Evolution of Placental Function in Mammals: The Molecular Basis of
1151 Gas and Nutrient Transfer, Hormone Secretion, and Immune Responses. Physiol Rev
1152 *92*, 1543-1576. 10.1152/physrev.00040.2011.

1153 10. Chen, Y., Siriwardena, D., Penfold, C., Pavlinek, A., and Boroviak, T.E. (2022). An
1154 integrated atlas of human placental development delineates essential regulators of
1155 trophoblast stem cells. Development *149*. 10.1242/dev.200171.

1156 11. Liu, Y., Fan, X., Wang, R., Lu, X., Dang, Y.L., Wang, H., Lin, H.Y., Zhu, C., Ge, H.,
1157 Cross, J.C., and Wang, H. (2018). Single-cell RNA-seq reveals the diversity of
1158 trophoblast subtypes and patterns of differentiation in the human placenta. Cell Res *28*,
1159 819-832. 10.1038/s41422-018-0066-y.

1160 12. Arutyunyan, A., Roberts, K., Troule, K., Wong, F.C.K., Sheridan, M.A., Kats, I., Garcia-
1161 Alonso, L., Velten, B., Hoo, R., Ruiz-Morales, E.R., et al. (2023). Spatial multiomics map
1162 of trophoblast development in early pregnancy. Nature *616*, 143-151. 10.1038/s41586-
1163 023-05869-0.

1164 13. Papuchova, H., Kshirsagar, S., Xu, L., Bougleux Gomes, H.A., Li, Q., Iyer, V., Norwitz,
1165 E.R., Strominger, J.L., and Tilburgs, T. (2020). Three types of HLA-G+ extravillous
1166 trophoblasts that have distinct immune regulatory properties. Proc Natl Acad Sci U S A
1167 *117*, 15772-15777. 10.1073/pnas.2000484117.

1168 14. Tilburgs, T., Crespo, A.C., van der Zwan, A., Rybalov, B., Raj, T., Stranger, B., Gardner,
1169 L., Moffett, A., and Strominger, J.L. (2015). Human HLA-G+ extravillous trophoblasts:
1170 Immune-activating cells that interact with decidual leukocytes. Proc Natl Acad Sci U S A
1171 *112*, 7219-7224. 10.1073/pnas.1507977112.

1172 15. Wallace, A.E., Fraser, R., and Cartwright, J.E. (2012). Extravillous trophoblast and
1173 decidual natural killer cells: a remodelling partnership. Hum Reprod Update *18*, 458-471.
1174 10.1093/humupd/dms015.

1175 16. Fuchs, R., and Ellinger, I. (2004). Endocytic and transcytotic processes in villous
1176 syncytiotrophoblast: role in nutrient transport to the human fetus. Traffic *5*, 725-738.
1177 10.1111/j.1600-0854.2004.00221.x.

1178 17. Robbins, J.R., Skrzypczynska, K.M., Zeldovich, V.B., Kapidzic, M., and Bakardjiev, A.I.
1179 (2010). Placental syncytiotrophoblast constitutes a major barrier to vertical transmission
1180 of Listeria monocytogenes. PLoS Pathog *6*, e1000732. 10.1371/journal.ppat.1000732.

1181 18. Shannon, M.J., McNeill, G.L., Koksal, B., Baltayeva, J., Wachter, J., Castellana, B.,
1182 Penaherrera, M.S., Robinson, W.P., Leung, P.C.K., and Beristain, A.G. (2024). Single-
1183 cell assessment of primary and stem cell-derived human trophoblast organoids as
1184 placenta-modeling platforms. Dev Cell *59*, 776-792 e711. 10.1016/j.devcel.2024.01.023.

1185 19. Friess, A.E., Sinowatz, F., Skolek-Winnisch, R., and Traautner, W. (1980). The placenta
1186 of the pig. I. Finestructural changes of the placental barrier during pregnancy. Anat
1187 Embryol (Berl) *158*, 179-191. 10.1007/BF00315905.

1188 20. McLendon, B.A., Kramer, A.C., Seo, H., Burghardt, R.C., Bazer, F.W., Wu, G., and
1189 Johnson, G.A. (2022). Temporal and spatial expression of aquaporins 1, 5, 8, and 9:
1190 Potential transport of water across the endometrium and chorioallantois of pigs. Placenta
1191 *124*, 28-36. 10.1016/j.placenta.2022.05.007.

1192 21. Stenhouse, C., Seo, H., Wu, G., Johnson, G.A., and Bazer, F.W. (2022). Insights into
1193 the Regulation of Implantation and Placentation in Humans, Rodents, Sheep, and Pigs.
1194 Adv Exp Med Biol *1354*, 25-48. 10.1007/978-3-030-85686-1_2.

1195 22. Friess, A.E., Sinowatz, F., Skolek-Winnisch, R., and Trautner, W. (1981). The placenta
1196 of the pig. II. The ultrastructure of the areolae. Anat Embryol (Berl) *163*, 43-53.
1197 10.1007/BF00315769.

1198 23. Roberts, R.M., Raub, T.J., and Bazer, F.W. (1986). Role of uteroferrin in transplacental
1199 iron transport in the pig. Fed Proc *45*, 2513-2518.

1200 24. Song, G., Bailey, D.W., Dunlap, K.A., Burghardt, R.C., Spencer, T.E., Bazer, F.W., and
1201 Johnson, G.A. (2010). Cathepsin B, cathepsin L, and cystatin C in the porcine uterus
1202 and placenta: potential roles in endometrial/placental remodeling and in fluid-phase

1203 transport of proteins secreted by uterine epithelia across placental areolae. Biol Reprod
1204 *82*, 854-864. 10.1095/biolreprod.109.080929.

1205 25. Zang, X., Zhang, D., Wang, W., Ding, Y., Wang, Y., Gu, S., Shang, Y., Gan, J., Jiang, L.,
1206 Meng, F., et al. (2024). Cross-Species Insights into Trophoblast Invasion During
1207 Placentation Governed by Immune-Featured Trophoblast Cells. Adv Sci (Weinh) *11*,
1208 e2407221. 10.1002/advs.202407221.

1209 26. Zang, X.P., Gu, S.C., Wang, W.J., Shi, J.S., Gan, J.Y., Hu, Q., Zhou, C., Ding, Y., He,
1210 Y.J., Jiang, L., et al. (2024). Dynamic intrauterine crosstalk promotes porcine embryo
1211 implantation during early pregnancy. Sci China Life Sci *67*, 1676-1696. 10.1007/s11427-
1212 023-2557-x.

1213 27. Jaeger, L.A., Spiegel, A.K., Ing, N.H., Johnson, G.A., Bazer, F.W., and Burghardt, R.C.
1214 (2005). Functional effects of transforming growth factor beta on adhesive properties of
1215 porcine trophectoderm. Endocrinology *146*, 3933-3942. 10.1210/en.2005-0090.

1216 28. Suleman, M., Malgarin, C.M., Detmer, S.E., Harding, J.C.S., and MacPhee, D.J. (2019).
1217 The porcine trophoblast cell line PTr2 is susceptible to porcine reproductive and
1218 respiratory syndrome virus-2 infection. Placenta *88*, 44-51.
1219 10.1016/j.placenta.2019.10.004.

1220 29. Ramsoondar, J., Christopherson, R.J., Guilbert, L.J., and Wegmann, T.G. (1993). A
1221 porcine trophoblast cell line that secretes growth factors which stimulate porcine
1222 macrophages. Biol Reprod *49*, 681-694. 10.1095/biolreprod49.4.681.

1223 30. Hou, D., Su, M., Li, X., Li, Z., Yun, T., Zhao, Y., Zhang, M., Zhao, L., Li, R., Yu, H., and
1224 Li, X. (2015). The Efficient Derivation of Trophoblast Cells from Porcine In Vitro Fertilized
1225 and Parthenogenetic Blastocysts and Culture with ROCK Inhibitor Y-27632. PLoS One
1226 *10*, e0142442. 10.1371/journal.pone.0142442.

1227 31. Kim, J., Koo, B.K., and Knoblich, J.A. (2020). Human organoids: model systems for
1228 human biology and medicine. Nat Rev Mol Cell Biol *21*, 571-584. 10.1038/s41580-020-
1229 0259-3.

1230 32. Yang, L., Liang, P., Yang, H., and Coyne, C.B. (2024). Trophoblast organoids with
1231 physiological polarity model placental structure and function. J Cell Sci *137*.
1232 10.1242/jcs.261528.

1233 33. Yang, L., Semmes, E.C., Ovies, C., Megli, C., Permar, S., Gilner, J.B., and Coyne, C.B.
1234 (2022). Innate immune signaling in trophoblast and decidua organoids defines
1235 differential antiviral defenses at the maternal-fetal interface. Elife *11*.
1236 10.7554/eLife.79794.

1237 34. Turco, M.Y., Gardner, L., Kay, R.G., Hamilton, R.S., Prater, M., Hollinshead, M.S.,
1238 McWhinnie, A., Esposito, L., Fernando, R., Skelton, H., et al. (2018). Trophoblast
1239 organoids as a model for maternal-fetal interactions during human placentation. Nature
1240 *564*, 263-267. 10.1038/s41586-018-0753-3.

1241 35. Keenen, M.M., Yang, L., Liang, H., Farmer, V.J., Singh, R., Gladfelter, A.S., and Coyne,
1242 C.B. (2024). Comparative analysis of the syncytiotrophoblast in placenta tissue and

trophoblast organoids using snRNA sequencing. bioRxiv, 2024.2007.2001.601571. 10.1101/2024.07.01.601571.

36. Caldwell, A., Yang, L., Scheef, E.A., Kaur, A., and Coyne, C. (2024). Comparative analysis of rhesus macaque and human placental organoids highlights evolutionary differences in placentation. bioRxiv, 2024.2010.2011.617873. 10.1101/2024.10.11.617873.

37. Haider, S., Meinhardt, G., Saleh, L., Kunihs, V., Gamperl, M., Kaindl, U., Ellinger, A., Burkard, T.R., Fiala, C., Pollheimer, J., et al. (2018). Self-Renewing Trophoblast Organoids Recapitulate the Developmental Program of the Early Human Placenta. Stem Cell Reports *11*, 537-551. 10.1016/j.stemcr.2018.07.004.

38. Guidoni, P.B., Pasternak, J.A., Hamonic, G., MacPhee, D.J., and Harding, J.C.S. (2021). Decreased tight junction protein intensity in the placenta of porcine reproductive and respiratory syndrome virus-2 infected fetuses. Placenta *112*, 153-161. 10.1016/j.placenta.2021.07.300.

39. Teixeira, S.A., Ibelli, A.M.G., Cantao, M.E., Oliveira, H.C., Ledur, M.C., Peixoto, J.O., Marques, D.B.D., Costa, K.A., Coutinho, L.L., and Guimaraes, S.E.F. (2019). Sex Determination Using RNA-Sequencing Analyses in Early Prenatal Pig Development. Genes (Basel) *10*. 10.3390/genes10121010.

40. Kramer, A.C., Steinhauser, C.B., Gao, H.J., Seo, H., McLendon, B.A., Burghardt, R.C., Wu, G.Y., Bazer, F.W., and Johnson, G.A. (2020). Steroids Regulate SLC2A1 and SLC2A3 to Deliver Glucose Into Trophectoderm for Metabolism via Glycolysis. Endocrinology *161*. ARTN bqaa098 10.1210/endocr/bqaa098.

41. Frank, J.W., Li, X.L., Erikson, D.W., Wu, G.Y., Bazer, F.W., Bayless, K.J., Burghardt, R.C., and Johnson, G.A. (2010). Expression of SPP1 (Osteopontin) and the Aggregation of Integrins into Focal Adhesions Is an Adaptation to Mechanical Forces at the Uterine-Placental Interface in Pigs. Biology of Reproduction, 147-147.

42. Kramer, A.C., Jansson, T., Bale, T.L., and Powell, T.L. (2023). Maternal-fetal cross-talk via the placenta: influence on offspring development and metabolism. Development *150*. 10.1242/dev.202088.

43. Lakhal-Littleton, S. (2021). Advances in understanding the crosstalk between mother and fetus on iron utilization. Semin Hematol *58*, 153-160. 10.1053/j.seminhematol.2021.06.003.

44. Lash, G.E. (2015). Molecular Cross-Talk at the Feto-Maternal Interface. Cold Spring Harb Perspect Med *5*. 10.1101/cshperspect.a023010.

45. Tian, Q., He, J.P., Zhu, C., Zhu, Q.Y., Li, Y.G., and Liu, J.L. (2022). Revisiting the Transcriptome Landscape of Pig Embryo Implantation Site at Single-Cell Resolution. Front Cell Dev Biol *10*. ARTN 796358 10.3389/fcell.2022.796358.

46. Cook, H.a.S.L. (2024). The United States Pork Industry 2023: Current Structure and Economic Importance. National Pork Producers Council. https://nppc.org/wp-content/uploads/2024/06/U.S.-Economic-Contribution-Report-6.28.24.pdf.

47. Bingying Liu, S.R., Hong An, Yixuan Liang, Xihui Sheng, Xiaolong Qi, Longfei Xiao, Xiangguo Wang (2024). Establishment of functional trophoblast organoids from trophoblast cells of bovine placenta. Cells & Development *Volume 180*. https://doi.org/10.1016/j.cdev.2024.203970.

48. Knight, J.W., Bazer, F.W., Thatcher, W.W., Franke, D.E., and Wallace, H.D. (1977). Conceptus Development in Intact and Unilaterally Hysterectomized-Ovariectomized Gilts - Interrelations among Hormonal Status, Placental Development, Fetal Fluids and Fetal Growth. J Anim Sci *44*, 620-637. DOI 10.2527/jas1977.444620x.

49. Amoroso, E.C., Hancock, N.A., Kellas, L. (1958). The Foetal Membranes and Placenta of the Hippopotamus (Hippopotamus amphibius (Linnaeus)). Proceedings of the Zoological Society of London *130*, 437-447.

50. Jones, C.J.P., Aplin, J.D., Salbany, A.C., Allen, W.R., and Wilsher, S. (2022). Observations on the glycosylation of the term placenta of the Indo-Pacific Bottlenose Dolphin ( ): A lectin histochemical study. Placenta *124*, 37-43. 10.1016/j.placenta.2022.05.013.

51. Iturrizaga, D.M., Verechia, F.T., Santos, T.C., Bombonato, P.P., Teixeira, D.G., and Miglino, M.A. (2007). The materno-fetal interface in llama ( ). Pesqui Vet Brasil *27*, 221-228. Doi 10.1590/S0100-736x2007000600001.

52. Keenen, M.M., Yang, L., Liang, H., Farmer, V.J., Singh, R., Gladfelter, A.S., and Coyne, C.B. (2024). Comparative analysis of the syncytiotrophoblast in placenta tissue and trophoblast organoids using snRNA sequencing. bioRxiv. 10.1101/2024.07.01.601571.

53. Chen, C.P., Liu, S.H., Lee, M.Y., and Chen, Y.Y. (2008). Heparan sulfate proteoglycans in the basement membranes of the human placenta and decidua. Placenta *29*, 309-316. 10.1016/j.placenta.2008.01.002.

54. Hong, L., Han, K., Wu, K., Liu, R., Huang, J., Lunney, J.K., Zhao, S., and Yu, M. (2017). E-cadherin and ZEB2 modulate trophoblast cell differentiation during placental development in pigs. Reproduction *154*, 765-775. 10.1530/REP-17-0254.

55. Kokkinos, M.I., Murthi, P., Wafai, R., Thompson, E.W., and Newgreen, D.F. (2010). Cadherins in the human placenta--epithelial-mesenchymal transition (EMT) and placental development. Placenta *31*, 747-755. 10.1016/j.placenta.2010.06.017.

56. Yen, I.W., Lin, S.Y., Lin, M.W., Lee, C.N., Kuo, C.H., Chen, S.C., Tai, Y.Y., Kuo, C.H., Kuo, H.C., Lin, H.H., et al. (2024). The association between plasma angiopoietin-like protein 4, glucose and lipid metabolism during pregnancy, placental function, and risk of delivering large-for-gestational-age neonates. Clin Chim Acta *554*, 117775. 10.1016/j.cca.2024.117775.

57. Wei, Q.Q., Li, R.Q., Zhong, L., Mu, H.Y., Zhang, S.P., Yue, L., Xiang, J.Z., Li, E.H., Zhi, M.L., Cao, S.Y., and Han, J.Y. (2018). Lineage specification revealed by single-cell gene

expression analysis in porcine preimplantation embryos. Biology of Reproduction *99*, 283-292. 10.1093/biolre/ioy062.

58. Ison, E.K., Kent-Dennis, C.E., Fazioli, J., Mulligan, M.K., Pham, A., and Pasternak, J.A. (2023). Compensatory mechanisms in response to induced hypothyroidism in the late gestation pig fetus. Biology of Reproduction *108*, 731-743. 10.1093/biolre/ioad024.

59. Hao, Y., Hao, S., Andersen-Nissen, E., Mauck, W.M., 3rd, Zheng, S., Butler, A., Lee, M.J., Wilk, A.J., Darby, C., Zager, M., et al. (2021). Integrated analysis of multimodal single-cell data. Cell *184*, 3573-3587 e3529. 10.1016/j.cell.2021.04.048.

60. Street, K., Risso, D., Fletcher, R.B., Das, D., Ngai, J., Yosef, N., Purdom, E., and Dudoit, S. (2018). Slingshot: cell lineage and pseudotime inference for single-cell transcriptomics. BMC Genomics *19*, 477. 10.1186/s12864-018-4772-0.

61. Van den Berge, K., Roux de Bezieux, H., Street, K., Saelens, W., Cannoodt, R., Saeys, Y., Dudoit, S., and Clement, L. (2020). Trajectory-based differential expression analysis for single-cell sequencing data. Nat Commun *11*, 1201. 10.1038/s41467-020-14766-3.

62. Ooms, J. (2023). magick: Advanced Graphics and Image-Processing in R.

63. Jin, S., Guerrero-Juarez, C.F., Zhang, L., Chang, I., Ramos, R., Kuan, C.H., Myung, P., Plikus, M.V., and Nie, Q. (2021). Inference and analysis of cell-cell communication using CellChat. Nat Commun *12*, 1088. 10.1038/s41467-021-21246-9.

64. Jin, S., Plikus, M.V., and Nie, Q. (2024). CellChat for systematic analysis of cell-cell communication from single-cell transcriptomics. Nat Protoc. 10.1038/s41596-024-01045-4.

65. Stuart, T., Butler, A., Hoffman, P., Hafemeister, C., Papalexi, E., Mauck, W.M., 3rd, Hao, Y., Stoeckius, M., Smibert, P., and Satija, R. (2019). Comprehensive Integration of Single-Cell Data. Cell *177*, 1888-1902 e1821. 10.1016/j.cell.2019.05.031.